Supplementary Information (SI) for Journal of Materials Chemistry A.

Combined Experimental and Theoretical Elucidation of PCET Pathways in Electrocatalytic Alcohol Oxidation and Its Application in PET Upcycling

Chetansinh Chauhan, Sanyam[#], Ram Sewak[#], Anirban Mondal[*], Biswajit Mondal[*]

Department of Chemistry, IIT Gandhinagar, Gujarat-382355, India

E-mail: mondal.biswajit@iitgn.ac.in

#Equally contributed

Experimental Procedures

Materials

All the chemical reagents were purchased from commercial sources and used without further purification. Benzyl alcohol, $CoCl_2.6H_2O$, 5-hydroxymethylfurfural (HMF) from Merck, and Potassium hydroxide (KOH) were purchased from Thermo Fisher Scientific India Pvt. LTD. D_2O, Benzene-1, 4-dicarboxylic acid (Terephthalic acid, TPA) were purchased from Sigma. (4-Methoxyphenyl) methanol, (4-chlorophenyl) methanol, (4-bromophenyl) methanol, 4-methyl benzylamine, 4-methoxy benzylamine and Ethane-d4-1,2-diol were purchased from BLD Pharmatech (India) Pvt. LTD. 4-Nitrobenzyl alcohol and hydrochloric acid (37 wt%) were purchased from Loba Chemie Pvt. LTD. DMSO-d6 from Eurisotop. Ethylene glycol was purchased from TCI, benzylamine from Novus, and 4-chlorobenzylamine from Ottokemi. Ni foam (NF) was purchased from Eliteck. Deionized water (18.2 MΩ cm resistivity at 25 °C, purified using a Millipore system) was used as the solvent for all the reported electrochemical experiments.

Characterization

The electrode surface characterization was performed by Field Emission Scanning Electron Microscopy (FE-SEM) with Jeol JSM7600F instrument and X-ray diffraction (XRD) with Bruker D8 DISCOVER instrument. X-ray photoelectron spectroscopy (XPS) analyses were performed on a Thermo Scientific K-Alpha X-ray Photoelectron spectrometer using Al Kα (1486.6 eV) X-ray radiation, and the data processing was performed using Avantage software.For liquid products, ^{1}H NMR and ^{13}C NMR were recorded on a Bruker Avance III 500 MHz spectrometer and The amount of produced hydrogen on the counter electrode was calculated using the GC-TCD method for the PET electrolysis.

Electrochemical Measurements

All the measurements were performed in a three-electrode system using *CHI 7044E* & Metrohm Autolab PGSTAT 101 potentiostat. Ag/AgCl (saturated KCl) and a Pt wire were used as the reference and counter electrodes. All the potentials were converted to the normal hydrogen electrode (NHE) scale:

$$E_{NHE}\ (V) = E_{Ag/AgCl} + 0.197 \qquad (\textit{Equation 1})$$

or to a reversible hydrogen electrode (RHE) scale using the Nernst equation at room temperature:

$$E_{RHE}\ (V) = E_{Ag/AgCl} + 0.0592 \times pH + 0.197 \qquad (\textit{Equation 2})$$

The scan rate for cyclic voltammetry (CV) and linear sweep voltammetry (LSV) measurements was maintained at 5 mV/s. A working electrode measuring 0.5×0.5 cm^2 of aCo BDC/NF, along with a platinum counter electrode and an Ag/AgCl reference electrode, was employed in an undivided cell. Measurements were conducted at room temperature using 1 M KOH (pH 14) as the electrolyte. The LSV curves in Figure 3a are iR corrected (70%).

A constant current of 100 mA cm^{-2} electrolysis was performed at room temperature with continuous stirring in an undivided cell. The working electrode was a 0.5×0.5 cm^2 of aCo BDC/NF, with platinum as the counter electrode and Ag/AgCl as the reference electrode, using a Metrohm Autolab PGSTAT 101 potentiostat. For PET electrolysis, a constant current of 50 mA cm^{-2} was applied using 0.5×1 cm^2 aCo BDC/NF for both the working and counter electrodes, with Ag/AgCl as the reference. This setup also utilized the Metrohm Autolab PGSTAT 101 potentiostat.

Electrochemical active surface area (ECSA) was determined from the following equation.

$$\mathrm{ECSA} = \left(\frac{C_{dl}}{C_s}\right) \times A_{geo} \qquad (\textit{Equation 3})$$

where the double layer capacitance, C_{dl} is determined from Figure S10, Specific capacitance, A_{geo} is the geometric surface area of the electrode (0.25 cm^2), and C_s was calculated using equation 7[1]:

$$C_s = \frac{1}{2A.\Delta V.\nu}\int_{V_1}^{V_2} I(V)dV \qquad (\textit{Equation 4})$$

where, A is the area of the electrode (in cm^2); V is the potential window (in V); ν is the scan rate (in V/s); I (V) is the current at voltage V (in A); V_1 and V_2 are the lower and upper potential limits of the CV scan.

% Faradaic yield (FY) and formate selectivity was determined from the following equations[2]:

$$\mathrm{FY}\ (\%) = \frac{Moles\ of\ product\ formed \times 96485\ C\ mol^{-1} \times n}{Total\ charge\ passed} \times 100\ \% \qquad (\textit{Equation 5})$$

where, *n* = is the number of moles of electrons transferred per mole of product[2]

$$\%\ Formate\ selectivity = \frac{\frac{Moles\ of\ produced\ formate}{2}}{Mole\ of\ converted\ EG} \times 100\ \% \qquad (\textit{Equation 6})$$

Turnover Frequency (TOF) and Turnover Number (TON) are determined using the following equation;[2,]

$$TOF = \frac{j \times N_A}{n \times F \times \tau} \qquad TON = TOF \times t \qquad (\textit{Equation 7})$$

Where, j = current density, N_A= Avogadro number, F = Faraday constant, n = Number of electrons, τ = number of surface-active sites and t = time.

The Nernst equation has been used to calculate the number of protons and electrons involved[3].

For a reaction, $mH^+ + ne^- \rightarrow \frac{m}{2}H_2$ $E = E^0 - \frac{0.059}{n} log\frac{1}{[H^+]^m}$ (*Equation 8*)

If $1H^+/2e^-$ process, then the equation will be, $E = E_0 - 0.059/2 \log 1/ [H^+]^1$, the slope would be $0.059/2 = 0.0295$ V $pH^{-1} \sim 30$ mV pH^{-1}

If $2H^+/1e^-$, process, then the equation will be, $E = E_0 - 0.059/1 \log 1/ [H^+]^2$, the slope would be $0.059x2 = 0.118$ V $pH^{-1} \sim 120$ mV pH^{-1}

The Hammett analysis was done in the mixed solvent with 2 mL of H_2O and 2 mL of acetonitrile (ACN) mixed with 30 mg of KOH, resulting in a solution with a pH of 14[4]. This adjustment was necessary since other Benzyl alcohol & Benzylamine derivatives were insoluble in 1 M KOH[4]. Cyclic voltammetry (CV) was subsequently conducted for each derivative. From the CVs, the k_x/k_H values were determined at a potential of 1.4 V. These values were then used to construct Hammett plots for the aNF & aCo BDC/NF catalysts.

Computational details

Methodology: All periodic DFT calculations were performed using the CP2K software package, employing the Gaussian and Plane Wave (GPW) method. Two distinct MOF slab models were investigated: (i) a pure Ni-based MOF and (ii) a mixed-metal MOF doped with Co, where both Co and Ni atoms were embedded in the framework. A slab model was constructed along the (100) crystallographic plane, consisting of two atomic layers. Adsorbates involved in the oxidation reactions were placed on a 2 × 2 in-plane supercell, as illustrated in Figure 1. To prevent spurious interactions between periodic images, a vacuum region of approximately 15 Å was introduced along the c-axis. The Perdew–Burke–Ernzerhof (PBE) functional within the generalized gradient approximation (GGA) was employed to describe exchange–correlation effects. Dispersion interactions were accounted for using the DFT-D3 method with a cutoff radius of 16 Å. A plane-wave cutoff of 500 Ry was used for the electronic density representation, with numerical accuracy controlled by an $EPS_{DEFAULT}$ of 1.0×10^{-10}. The electronic self-consistent field (SCF) procedure employed the orbital transformation (OT) method with a conjugate gradient (CG) minimizer and a full single inverse preconditioner, with convergence thresholds set to 10^{-6} for change in electronic density during inner and outer SCF

calculations. All atoms were described using DZVP-MOLOPT-SR-GTH basis sets and GTH pseudopotentials. The d-band center (ε_e) was calculated from the projected density of states (PDOS) using the following equation: (*Equation S9*)

$$\varepsilon_e = [\ \int E \times D_e(E)\ dE\ ] / [\ \int D_e(E)\ dE\ ]$$

Here, $D_e(E)$ is the density of d-states at energy E. The integration was performed over the energy range from -8 eV to +2.5 eV, covering a significant portion of the d-band contributions near the Fermi level.

Electrochemical oxidation processes-particularly the Ni^{2+}/Ni^{3+} transformation-are intrinsically governed by proton-coupled electron transfer (PCET) mechanisms, which are not fully captured within a simplified one-electron DFT framework. Consequently, the relatively high oxidation barriers obtained in this study should be viewed in light of these methodological limitations. Additionally, the use of semi-empirical methods (e.g., XTB) for initial transition-state estimation can lead to systematic overestimation of barrier heights. Nonetheless, since the primary objective of this work is to establish comparative mechanistic trends between the two catalytic systems rather than to predict absolute oxidation potentials, the relative energetics and the resulting qualitative conclusions remain robust and physically meaningful.

The entropy of adsorbed species is substantially reduced relative to their gas-phase counterparts due to the severe restriction of translational and rotational degrees of freedom upon surface binding. Consequently, elementary steps involving surface-bound intermediates, particularly those that are strongly stabilised, can exhibit pronounced exergonic free energy changes. Such trends are well documented in density functional theory studies of heterogeneous catalysis that employ surface-bound reference states.[5]

The transition-state calculations in this study are carried out within a constant-charge (fixed-electron) framework. This approach is appropriate for the present analysis, which emphasizes relative activation barriers to elucidate comparative mechanistic trends between the catalytic systems and is consistent with the experimentally observed kinetic behavior.

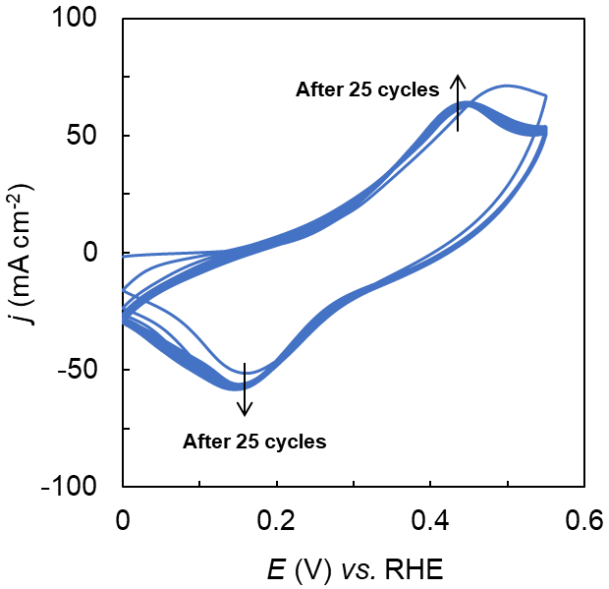

Figure S1. Electrochemical activation of Co BDC/NF. 25 CV scans at 10 mV/s for the activation of Co BDC/NF in 1 M KOH with 0.5×0.5 cm^2 Co BDC/ NF as the working electrode, Pt as the counter electrode, and Ag/ AgCl as the reference electrode in an undivided cell, at room temperature.

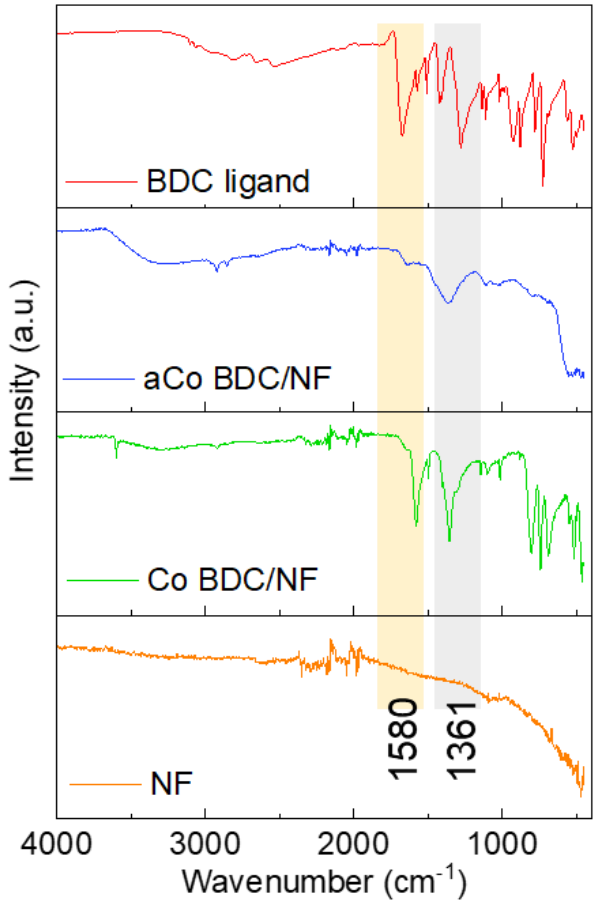

Figure S2. FTIR spectra of Co BDC/NF before and after electrochemical activation. FTIR spectra of Ni foam (orange), as-prepared Co BDC/NF (green), activated Co BDC/NF (blue), and BDC ligand (red).

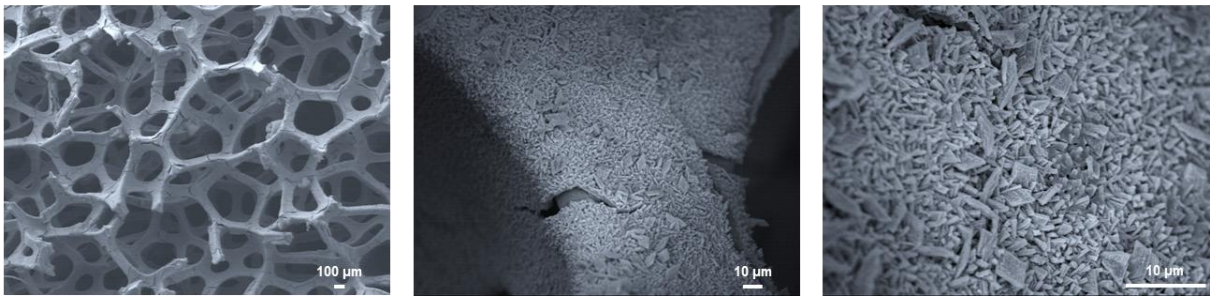

Figure S3. FE-SEM images of aCo BDC/NF. FE-SEM images of aCo BDC/NF at different magnifications.

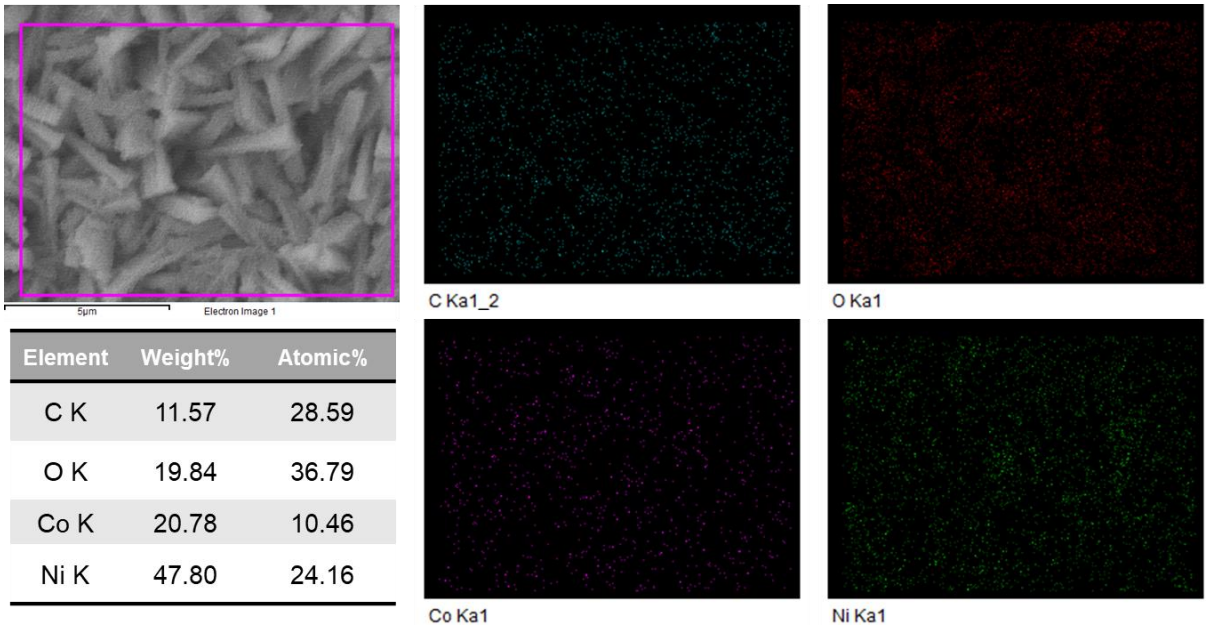

Element	Weight%	Atomic%
C K	11.57	28.59
O K	19.84	36.79
Co K	20.78	10.46
Ni K	47.80	24.16

Figure S4. Elemental mapping and EDS% composition (FE-SEM) of aCo BDC/NF using FE-SEM. SEM data and corresponding element mapping: C: cyan, O: red, Co: magenta, Ni: green.

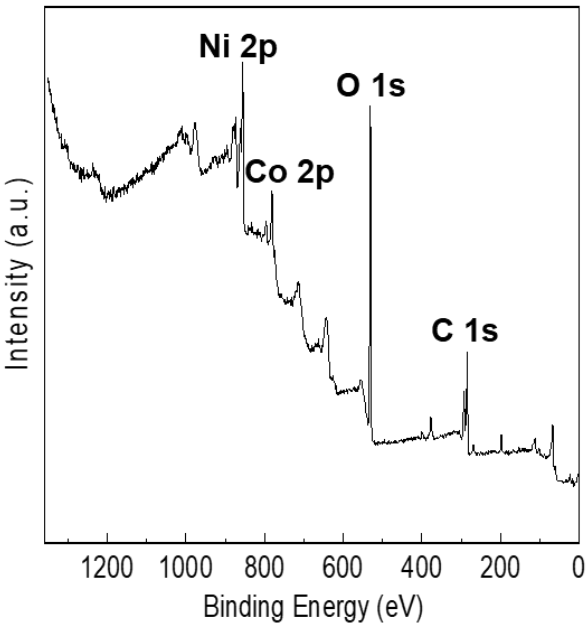

Figure S5. XPS survey spectra of aCo BDC/NF. XPS of aCo BDC/NF.

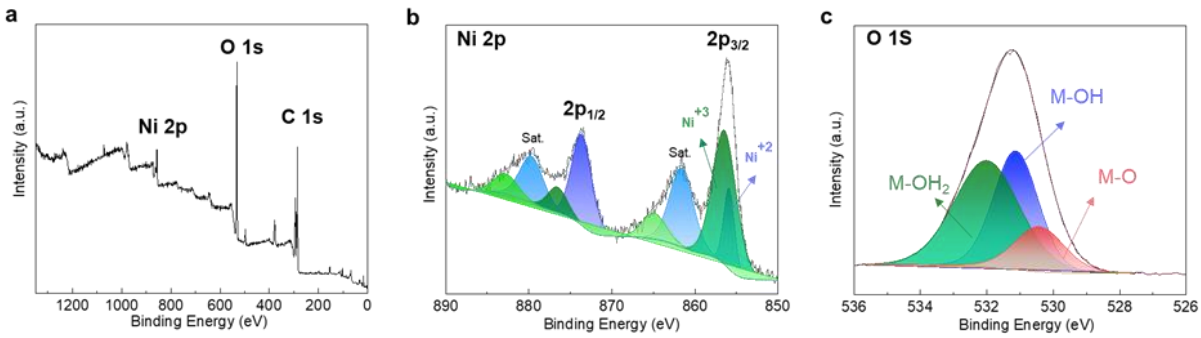

Figure S6. XPS spectra of aNF. a) XPS survey spectra; b) XPS spectra of Ni 2p; c) XPS spectra of O 1s; of aNF.

Supplementary note-1

High-resolution XPS spectra for Ni 2p and O 1s are shown in **Figure S6**. For Ni, prominent peaks at 855.86 eV and 873.6 eV correspond to the $2p_{3/2}$ and $2p_{1/2}$ states of Ni^{2+}, while peaks at 856.4 eV and 876.5 eV correspond to the $2p_{3/2}$ and $2p_{1/2}$ states of Ni^{3+}, as shown in **Figure S6b**. These distinct deconvoluted peaks confirm the presence of Ni^{3+}. Broad satellite features (designated as "sat.") are observed between 861-865 eV and 879-883 eV for the $2p_{3/2}$ and $2p_{1/2}$ states, respectively. The area ratios of these peaks, Ni^{3+}: Ni^{2+}, are 3.6:1. Additionally, the O 1s spectrum (**Figure S6c**) reveals peaks at 532.14 eV, 531.1 eV, and 530.3 eV, which correspond to M-OH_2, M-OH, and M-O (M = Ni) species, respectively. The area ratios of these peaks (M-OH_2: M-OH: M-O) for the aNF catalyst are 1:0.76:0.31.

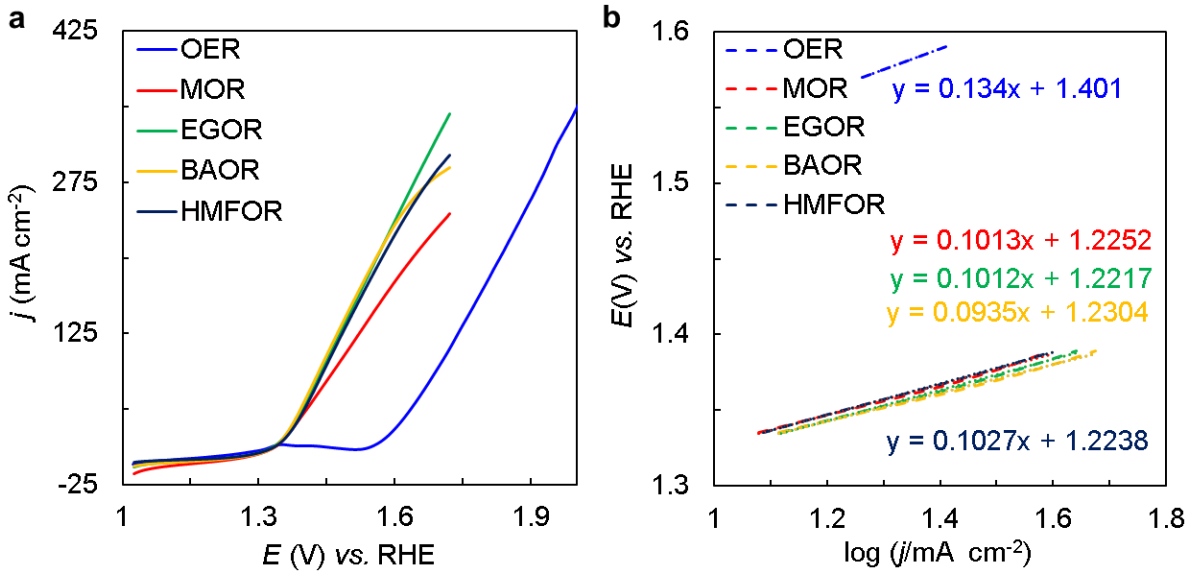

Figure S7. Electrochemical Analysis for Various Alcohol Oxidation: a) Comparison of LSVs for the catalyst during OER, Methanol (M), ethylene glycol (EG), Benzyl alcohol (BA), and 5-hydroxymethylfurfural (HMF) (each 100 mM) oxidation in 1 M KOH; b) Tafel slope analysis for OER, MOR, EGOR, BAOR, and HMFOR; 0.5×0.5 cm^2 aCo BDC/NF as the working electrode, Pt as the counter electrode, and Ag/AgCl as the reference electrode in an undivided cell, at room temperature; without iR correction; Ref: Figure 3.

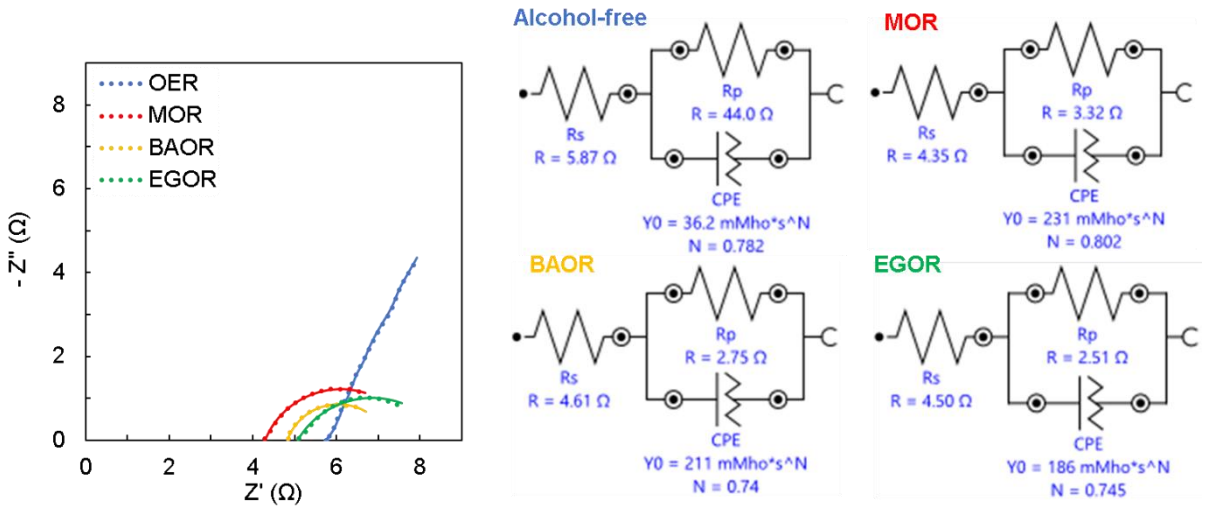

Figure S8. EIS analysis of aCo BDC/NF in the absence of alcohol and during AORs. Electrochemical impedance measurement with Nyquist plot and respective circuit fitting diagram for aCo BDC/ NF during Alcohol-free (R_{ct} = 44 Ω), MOR (R_{ct} = 3.32 Ω), BAOR (R_{ct} = 2.75 Ω), & EGOR (R_{ct} =2.51 Ω) (100 mM each) conducted in 1 M KOH across a frequency range of 0.1 to 10^5 Hz with an amplitude of 0.01 at 1.42 V *vs.* RHE; 0.5×0.5 cm^2 aCo BDC/NF as the working electrode, Pt as the counter electrode, and Ag/AgCl as the reference electrode in an undivided cell, at room temperature.

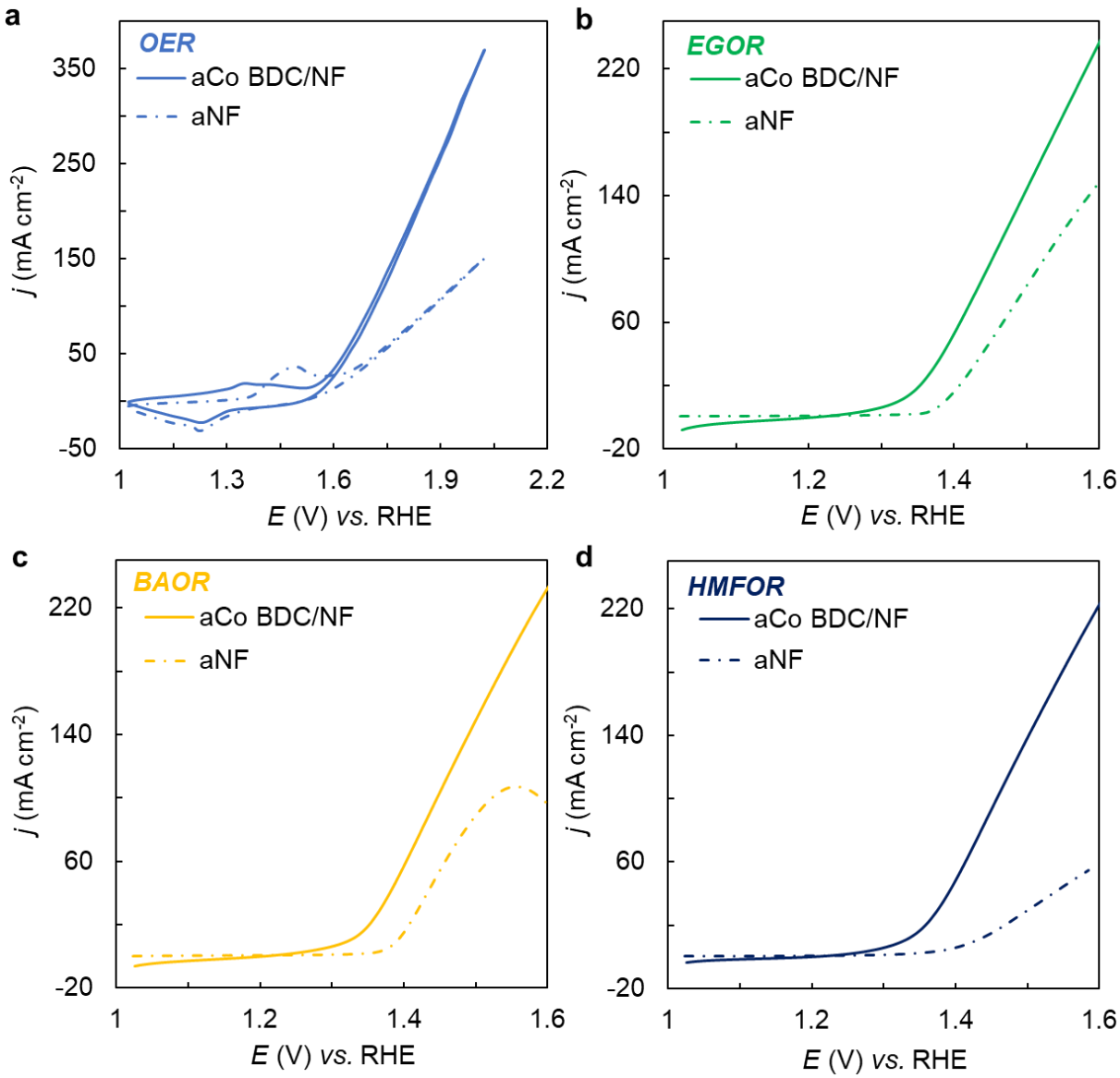

Figure S9. Electrochemical OER, EGOR, BAOR, and HMFOR comparison using aNF[4] and aCO BDC/NF. LSVs for the catalyst comparison of aNF and aCo BDC/NF during a) OER; b) 100 mM ethylene glycol (EG) oxidation; c) 100 mM Benzyl alcohol (BA) oxidation; and d) 100 mM 5-hydroxymethylfurfural (HMF) oxidation; in 1 M KOH; using 0.5×0.5 cm^2 aCo BDC/ NF as the working electrode, Pt as the counter electrode, and Ag/ AgCl as the reference electrode in an undivided cell, at room temperature.

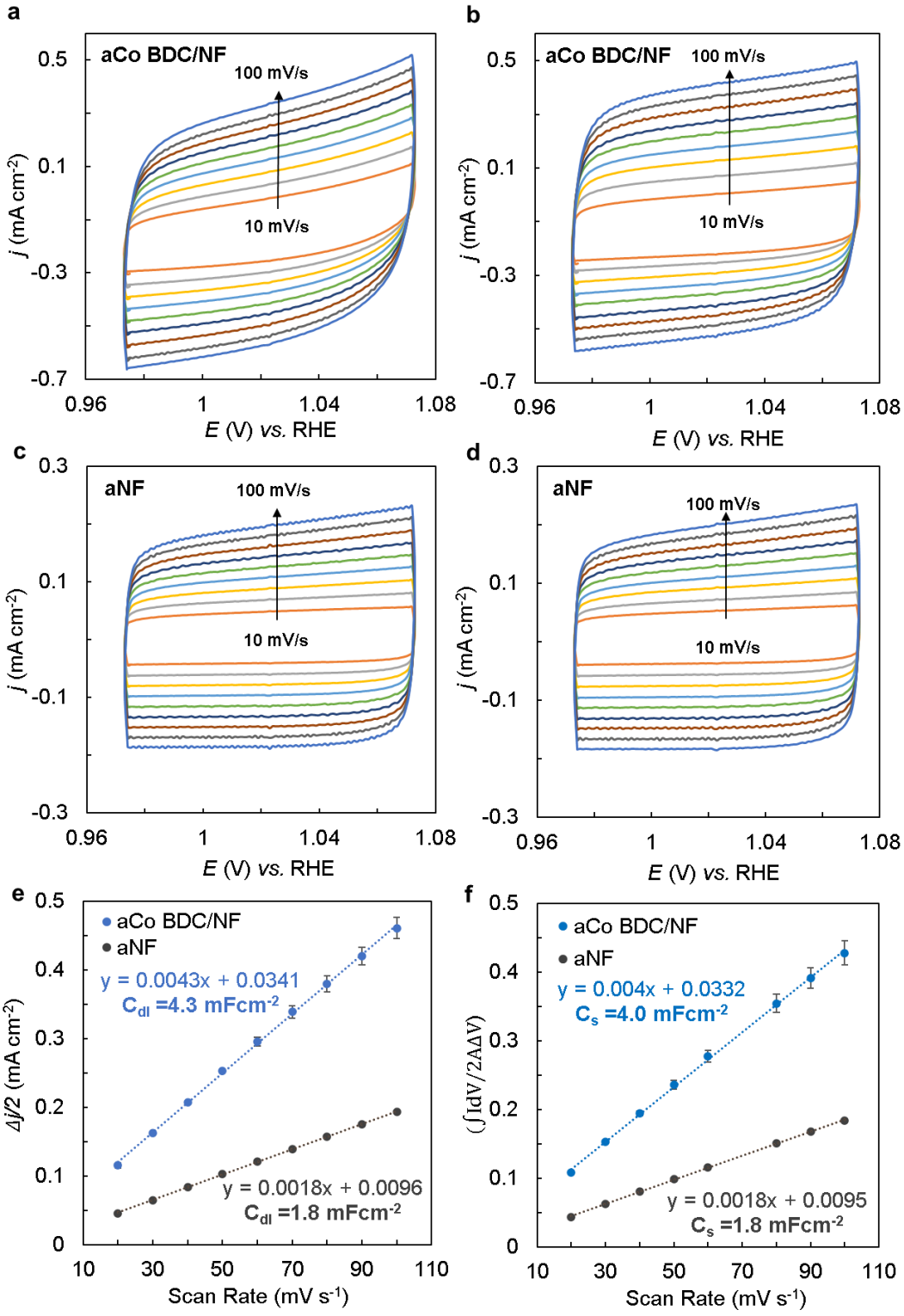

Figure S10. Electrochemical characterization and ECSA measurements of the aCo BDC/NF and aNF. Scan rate-dependent CVs in the non-Faradaic region in 1 M KOH of a, b) aCo BDC/NF; c, d) aNF; e) C_{dl} measurement at different scan rates ranging from 20 to 100 mVs^{-1}; f) Specific capacitance (C_s) measurement at different scan rates ranging from 20 to 100 mVs^{-1}; using 0.5×0.5 cm^2 aCO BDC/NF or aNF as the working electrode, Pt as the counter electrode, and Ag/ AgCl as the reference electrode in an undivided cell, at room temperature.

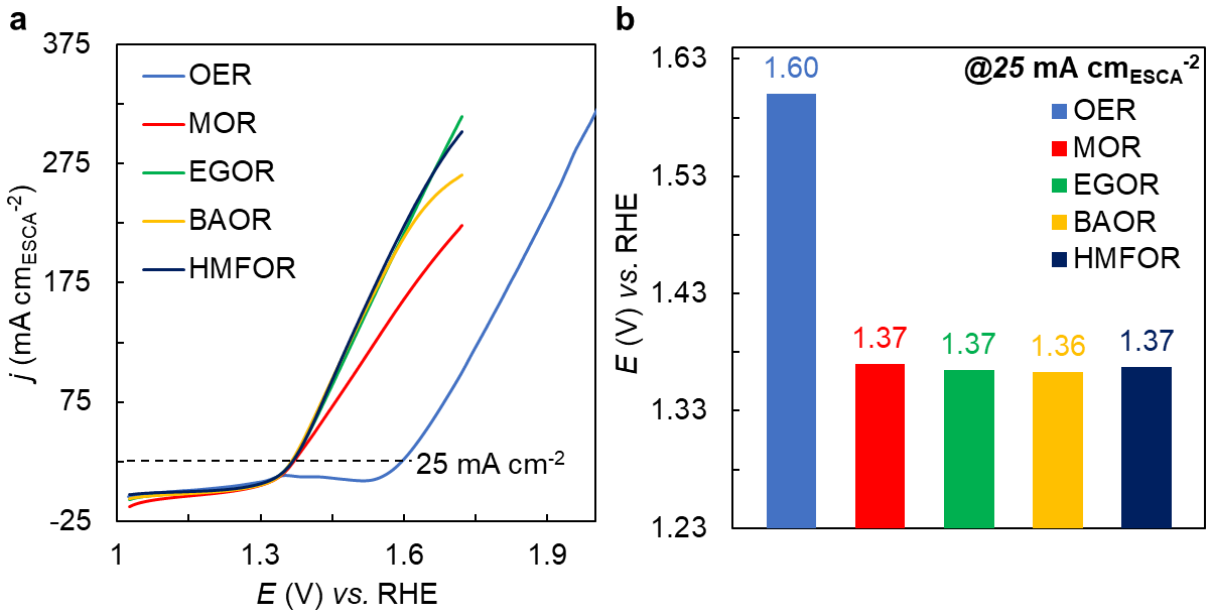

Figure S11. ECSA normalized current density for OER, MOR, EGOR, BAOR, and HMFOR using aCo BDC/NF. a) Comparative ECSA normalized LSVs of OER, 100 mM MeOH, 100 mM EG, 100 mM BA, and 100 mM HMF in 1 M KOH, b) potential requirements to produce 25 $mAcm^{-2}$ specific current density (ECSA normalized); using 0.5×0.5 cm^2 aCo BDC/NF as the working electrode, Pt as the counter electrode, and Ag/ AgCl as the reference electrode in an undivided cell, at room temperature.

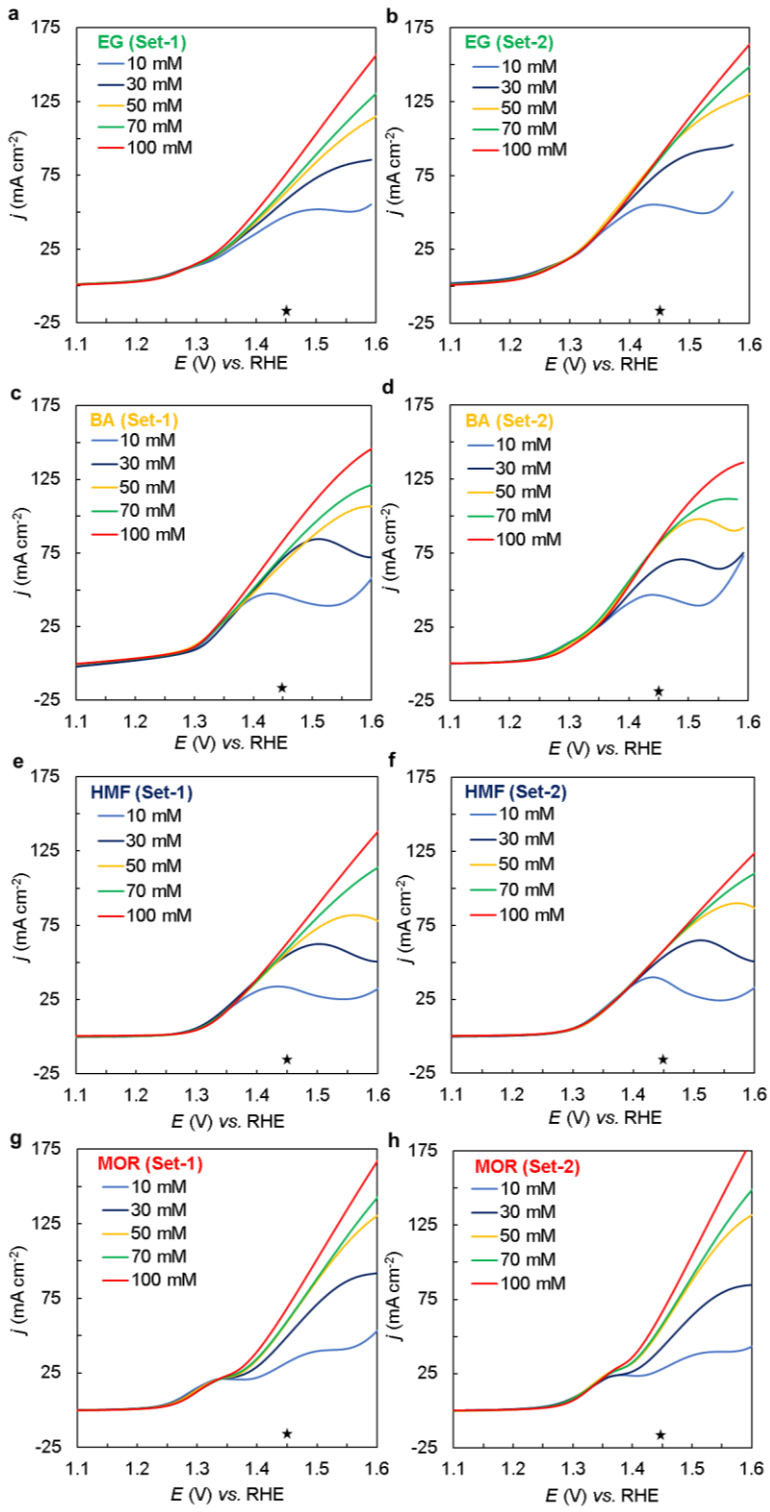

Figure S12. Electrochemical kinetic studies of AORs by aCo BDC/NF. LSVs at varying substrate concentrations (10–100 mM) in 1 M KOH; a, b) varied EG concentrations; c, d) varied BA concentrations; e, f) varied HMF concentrations g, h) varied HMF concentrations; i) log(j) *vs.* log(c) plots for different substrates; 0.5×0.5 cm^2 aCo BDC/NF as the working electrode, Pt as the counter electrode, and Ag/AgCl as the reference electrode in an undivided cell, at room temperature.

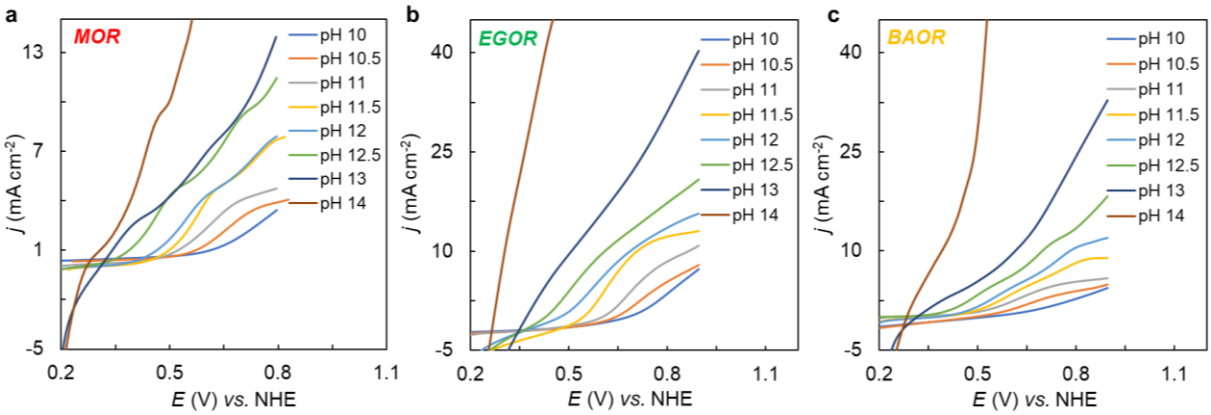

Figure S13. Electrochemical pH-dependence of SOR by aCo BDC/NF. LSVs of a) 100 mM MOR; b) 100 mM EGOR; and c) 100 mM BAOR; at different pH values (10, 10.5 11, 11.5, 12, 12.5, 13 and 14), 0.5×0.5 cm^2 activated Co BDC/NF as the working electrode, Pt as the counter electrode, and Ag/AgCl as the reference electrode in an undivided cell, at room temperature.

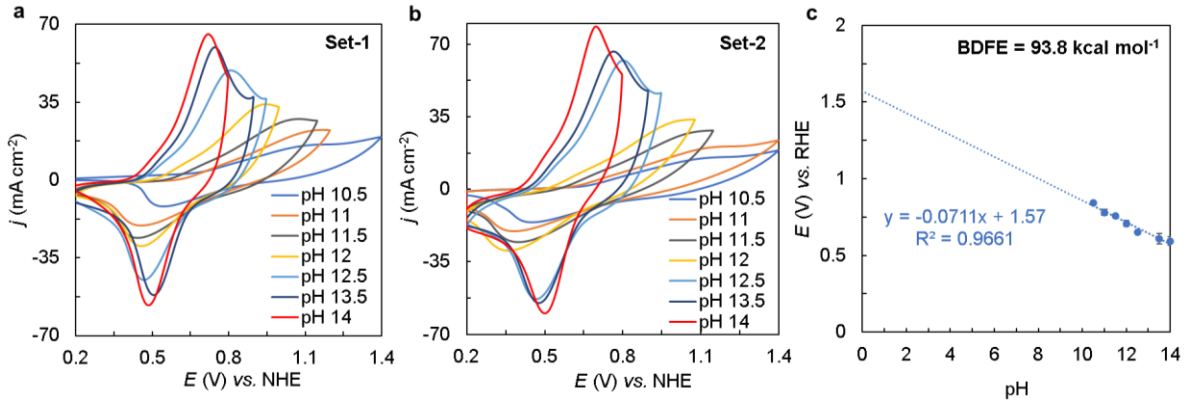

Figure S14. Electrochemical characterization of the activated Co BDC/NF. a) CV of activated Ni BDC/ NF at different pH values (10.5, 11, 11.5 12, 12.5, 13.5, and 14); b) $E_{1/2}$ *vs.* pH plot to determine the BDFE; using 0.5×0.5 cm^2 aCo BDC/NF as the working electrode, Pt as the counter electrode, and Ag/ AgCl as the reference electrode in an undivided cell, at room temperature;

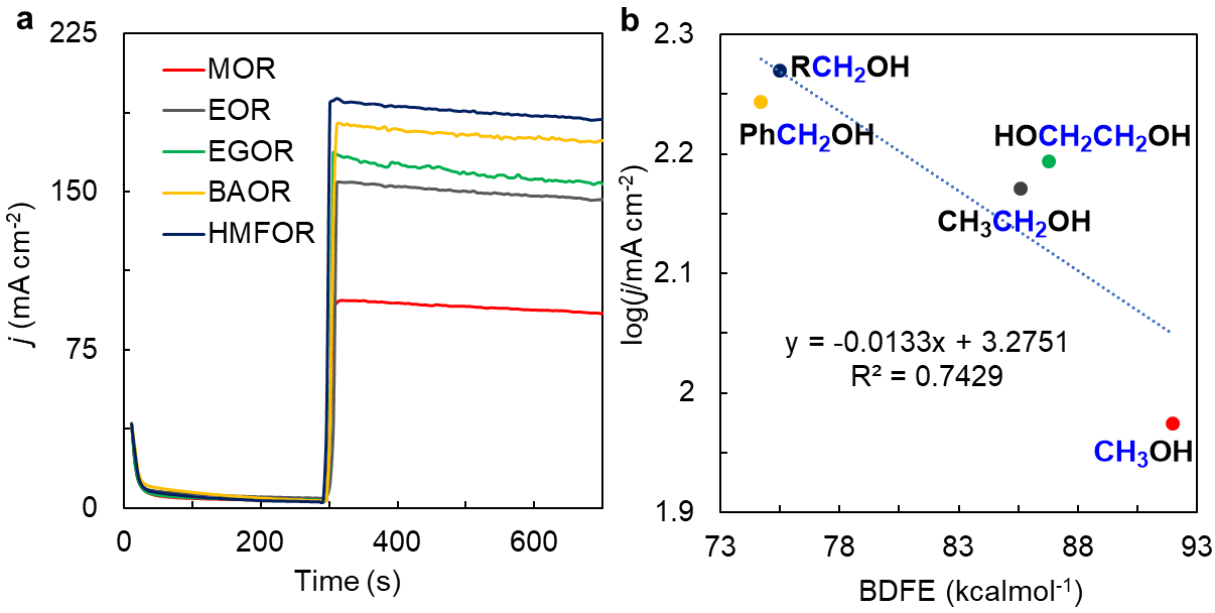

Figure S15. Electrochemical characterization of the aCo BDC/NF. a) Chronoamperometry at 1.37 V for MOR, EOR, EGOR, BAOR, and HMFOR (100 mM each) in 1 M KOH; b) log (*j*/mA cm^{-2}) *vs.* BDFE (kcal mol^{-1}) plot; using 0.5×0.5 cm^2 aCo BDC/NF as the working electrode, Pt as the counter electrode, and Ag/ AgCl as the reference electrode in an undivided cell, at room temperature;

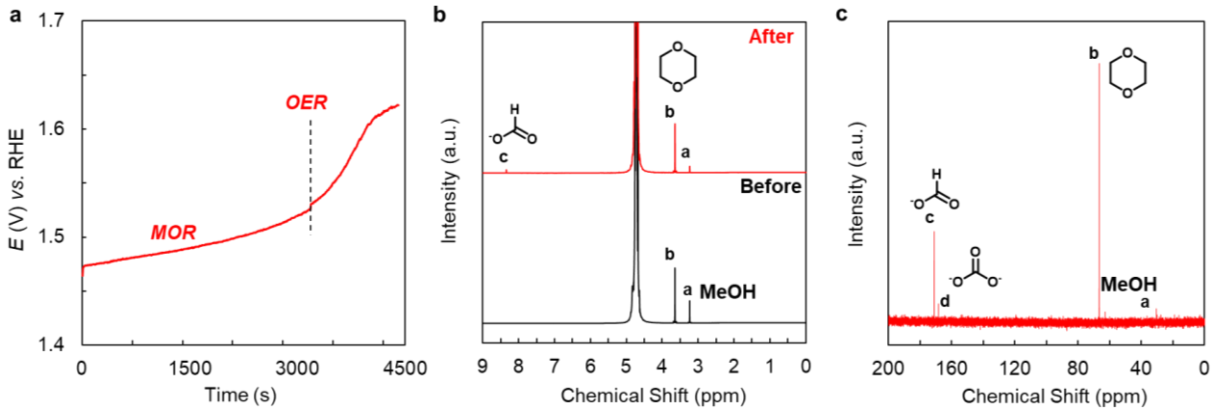

Figure S16. Chrono-potentiometry for MOR & electrolysis product characterization.

a) 4 mL 1 M KOH aqueous solution was used as electrolyte with 100 mM MeOH, and the electrolysis was performed at a constant current of 100 mA cm^{-2} in an undivided cell, b) ^{1}H-NMR spectrum of MeOH oxidation before and after constant current electrolysis; c) ^{13}C-NMR spectrum after constant current electrolysis. NMR spectra are reported in D_2O solvent, and 1,4-dioxane (3.6 ppm) was used as the internal standard for the product quantification.

Supplementary note-2

An aliquot was collected at 4400 s (110 C) for MOR, and the Faradaic efficiency (FE) for formate was determined to be 85%. The electrolyte was analyzed using ^{1}H-NMR in D_2O, showing formate formation at 8.31 ppm. Product quantification was performed using 1,4-dioxane as an internal standard. Additionally, trace amounts of carbonate resulting from formate over-oxidation were identified in ^{13}C-NMR spectra.

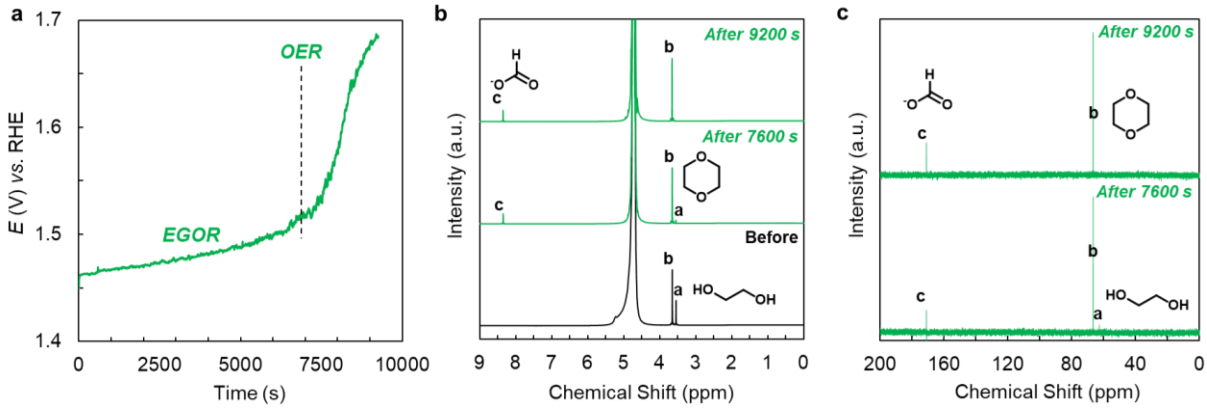

Figure S17. Chrono-potentiometry for EGOR & electrolysis product characterization. a) 4 mL 1 M KOH aqueous solution was used as electrolyte with 100 mM EG, and the electrolysis was performed at a constant current of 100 mA cm^{-2} in an undivided cell, b) ^{1}H-NMR spectrum of EG oxidation before and after constant current electrolysis; c) ^{13}C-NMR spectrum after constant current electrolysis. NMR spectra are reported in D_2O solvent, and 1,4-dioxane (3.6 ppm) was used as the internal standard for the product quantification.

Supplementary note-3

An aliquot was collected at 7600 s (190 C) for EGOR, with a formate selectivity of 91% and an FE of 99%. By the end of the reaction at 9200 s (231 C), the formate selectivity had decreased to 78%, and the FE dropped to 79%. The formation of formate was confirmed via ^{1}H-NMR in D_2O, showing a signal at 8.31 ppm. Product quantification was conducted using 1,4-dioxane as an internal standard, while ^{13}C-NMR spectra revealed trace carbonate formation due to formate over-oxidation.

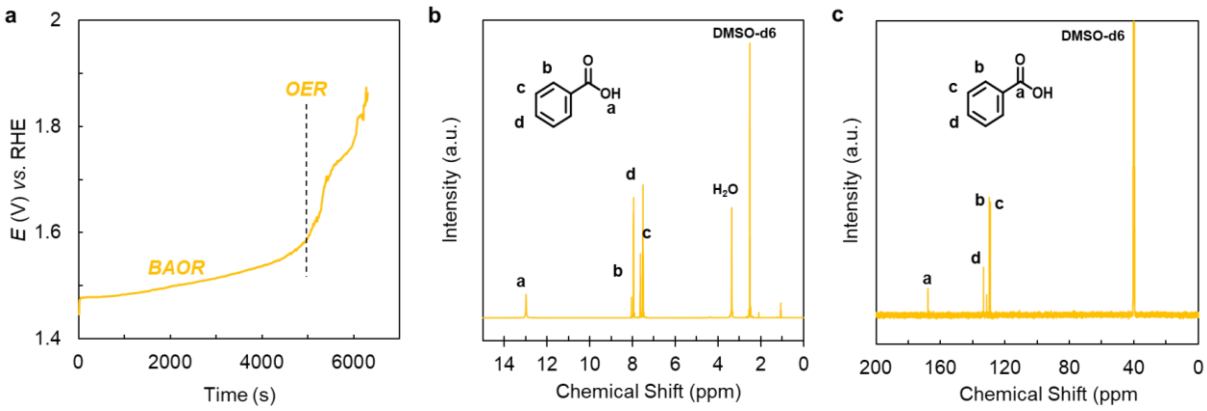

Figure S18. Chrono-potentiometry for BAOR & electrolysis product characterization.

a) 4 mL 1 M KOH aqueous solution was used as electrolyte with 100 mM BA, and the electrolysis was performed at a constant current of 100 mA cm^{-2} in an undivided cell; b) ^{1}H-NMR spectrum of BAOR oxidation isolated product (benzoic acid) after constant current electrolysis; c) ^{13}C-NMR spectrum. NMR spectra are reported in the DMSO-d^{6} solvent.

Supplementary note-4

For BAOR, ~155 C of charge was passed over 6200 s, leading to benzoic acid precipitation after acidifying the electrolyte under cold conditions. The isolated yield was calculated, and product characterization was performed using ^{1}H-NMR and ^{13}C-NMR. The aCo BDC/NF catalyst achieved an FE of 95% for this reaction.

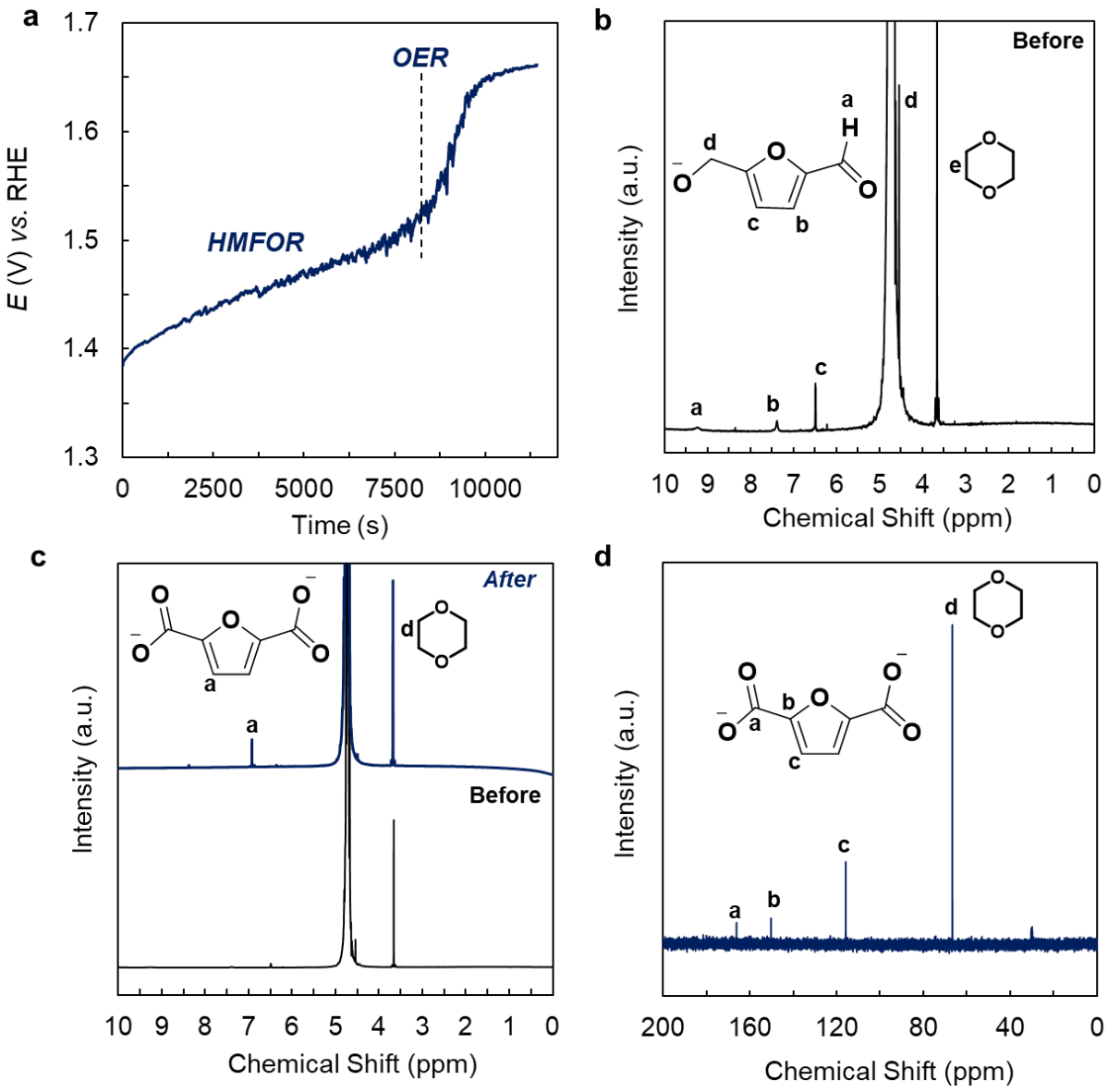

Figure S19. Chrono-potentiometry for HMFOR & electrolysis product characterization. a) 5 mL 1 M KOH aqueous solution was used as electrolyte with 100 mM HMF, and the electrolysis was performed at a constant current of 100 mA cm^{-2} in an undivided cell; b) ^{1}H-NMR spectrum of HMF oxidation before constant current electrolysis; c) ^{1}H-NMR spectrum of HMF oxidation before and after constant current electrolysis; d) ^{13}C-NMR spectrum after constant current electrolysis. NMR spectra are reported in D_2O solvent, and 1,4-dioxane (3.6 ppm) was used as the internal standard for the product quantification.

Supplementary note-5

For HMFOR, an aliquot was taken at 11,500 s (287 C), where the Faradaic efficiency for 2,5-furan-dicarboxylic acid (FDCA) was determined to be 84%. Product quantification was conducted using 1,4-dioxane as an internal standard in ^{1}H-NMR and ^{13}C-NMR in D_2O.

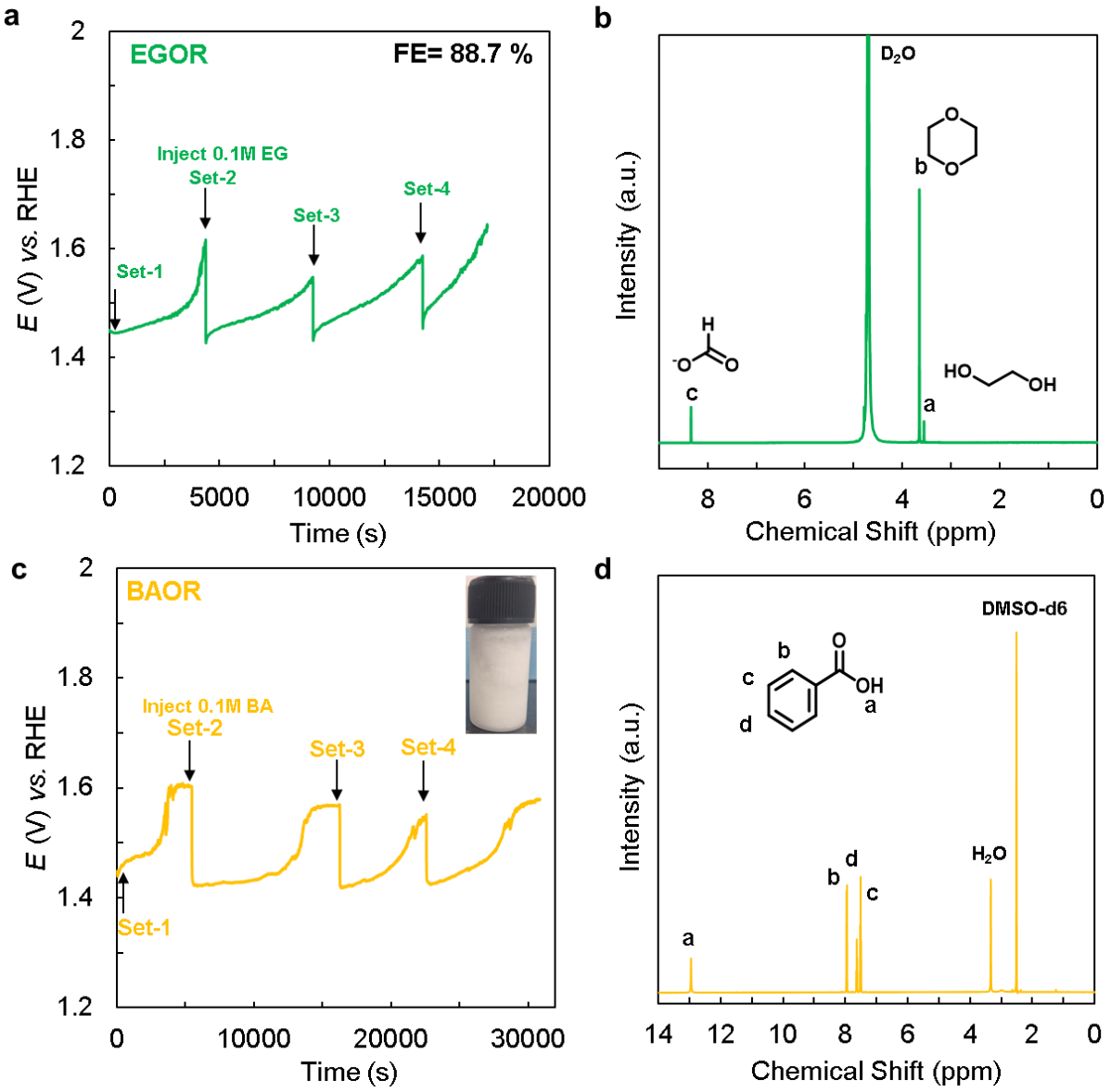

Figure S20. Catalyst recyclability and product analysis for EGOR and BAOR. a) Chrono-potentiometric stability test for EGOR in 4 mL 1 M KOH with 100 mM EG at 100 mA cm^{-2} in an undivided cell. The catalyst shows stable operation over four consecutive cycles with periodic injection of EG (total electrolysis time 16500 s, Q = 825 C); 4.82±0.12 ppb Co and 114.15±0.92 ppb Ni were obtained through ICP-MS in the post-electrolysis electrolyte sample; b) ^{1}H-NMR spectrum of the EGOR electrolyte after electrolysis recorded in D_2O using 1,4-dioxane (3.6 ppm) as the internal standard, giving an overall Faradaic efficiency of 88.7%; c) Chrono-potentiometric stability test for BAOR in 5 mL 1 M KOH with 100 mM BA at 100 mA cm^{-2} over four cycles, demonstrating good recyclability; inset: recovered solid benzoic acid; d) ^{1}H-NMR spectrum of the BAOR product confirming benzoic acid, which was recovered in 90.6% yield after electrolyte acidification.

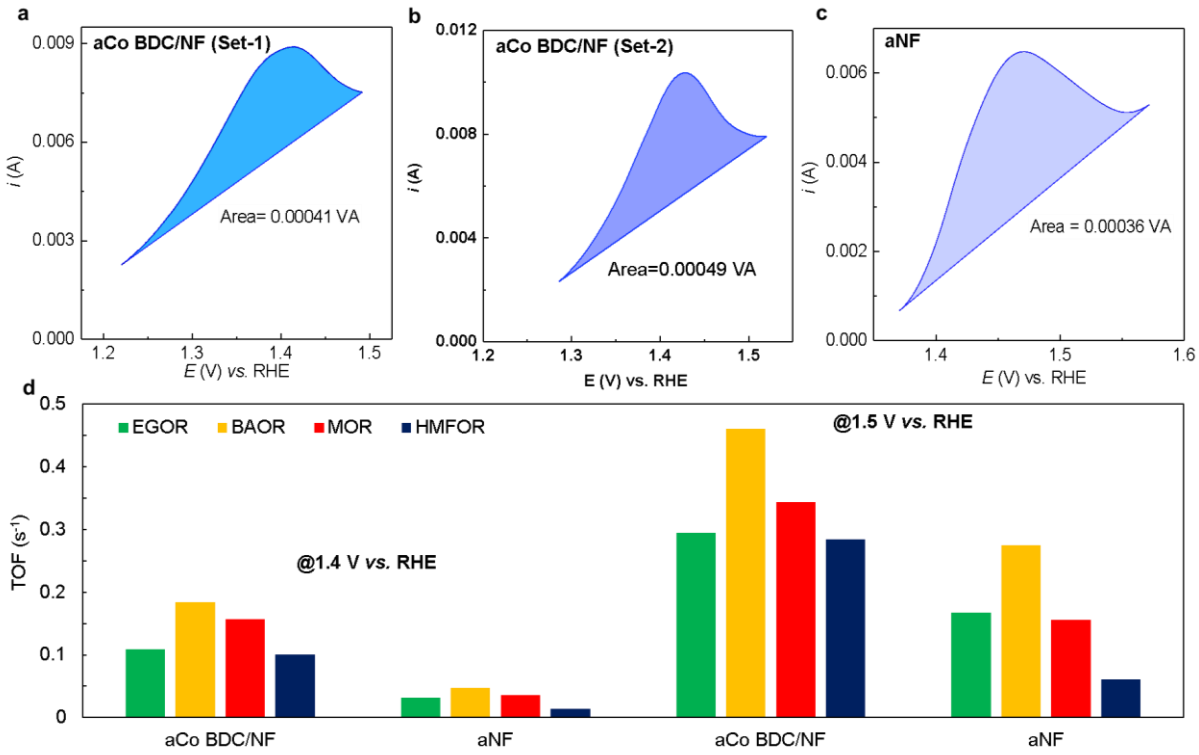

Figure S21. Comparison of turnover frequency (TOF) values for MOR, EGOR, BAOR, and HMFOR using aCo BDC/NF and aNF catalysts. Oxidation area corresponding to Ni^{2+} to Ni^{3+} conversion of a, b) aCo BDC/NF; c) aNF; d) bar chart illustrating the TOF values achieved by aCo BDC/NF and aNF catalysts at applied potentials of 1.4 V and 1.5 V vs. RHE. Measurements were conducted in 1.0 M KOH containing 100 mM of each substrate, using a 0.5 × 0.5 cm^2 aCo BDC/NF electrode as the working electrode, Pt as the counter electrode, and Ag/AgCl as the reference electrode in an undivided cell at room temperature.

Table S1. Turnover Number (TON) and Turnover Frequency (TOF) for the alcohol oxidation reactions.

At 100 mA cm^{-2}	TOF (s^{-1})	TON
MOR	0.28 ± 0.03	1232
EGOR	0.18 ± 0.02	1418
BAOR	0.28 ± 0.03	1736
HMFOR	0.18 ± 0.02	2146

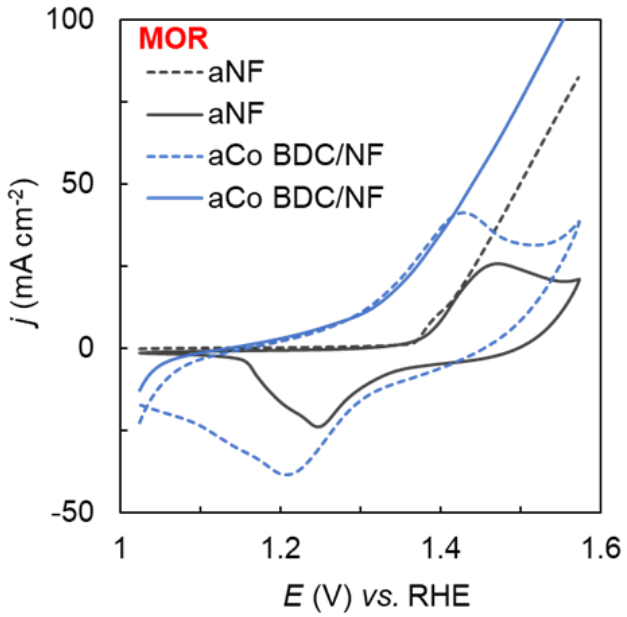

Figure S22. CV of aCo BDC/NF and aNF in 1M KOH (dashed line) and LSV of aCo BDC/NF and aNF in 100 mM MeOH/1M KOH. 0.5×0.5 cm^2 aCo BDC/NF as the working electrode, Pt as the counter electrode, and Ag/AgCl as the reference electrode in an undivided cell, at room temperature.

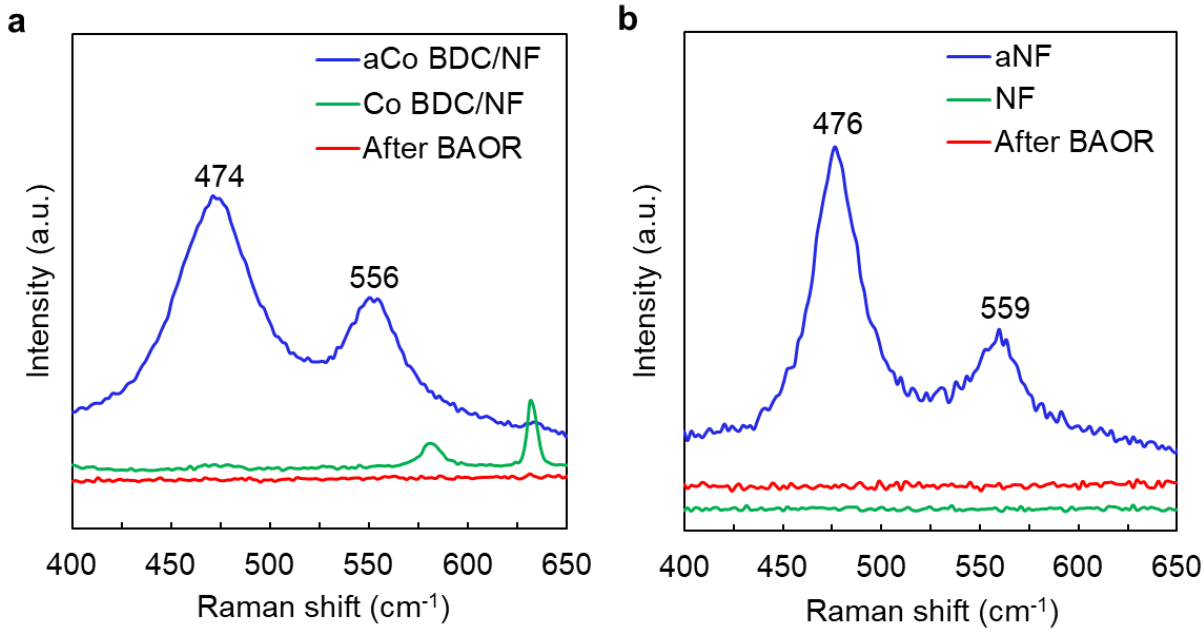

Figure S23. Raman spectra of Co BDC/NF and NF before and after activation and BAOR. **a)** Raman spectra of Co BDC/NF before activation (green), after electrochemical activation to aCo BDC/NF (blue), confirming the formation of Ni^{3+}(O)OH species, and after benzyl alcohol oxidation reaction (BAOR) (red), indicating the spontaneous reduction of Ni(O)OH in the presence of benzyl alcohol; **b)** Raman spectra of NF before activation (green), after electrochemical activation to aNF (blue), confirming Ni^{3+}(O)OH formation, and after BAOR (red), again evidencing spontaneous reduction of Ni(O)OH during alcohol oxidation.

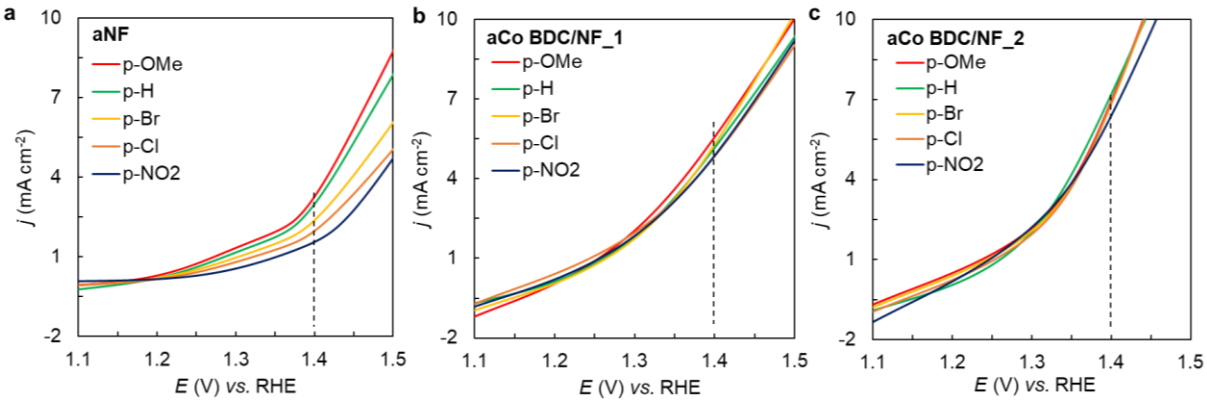

Figure S24. Hammett analysis of aNF and aCo BDC/NF for BAOR. LSVs of a) aNF; b) set-1of aCo BDC/NF; c) set-2 of aCo BDC/NF; for 100 mM BAOR with different *p*-substituents on BA in a mixed solvent (MeCN+H_2O+KOH) and Hammett analysis done at 1.4 V; 0.5×0.5 cm^2 activated NF and Co BDC/NF as the working electrode, Pt as the counter electrode, and Ag/AgCl as the reference electrode in an undivided cell, at room temperature. (σ values of *p*-substituents -OMe, -Br, -Cl, and -NO_2 are -0.27, 0.23,0.23 and 0.78, respectively).

Table S2. Literature reported for the hydrogen atom transfer (HAT) pathway using Hammett studies.

Catalyst	ρ value	Mechanism	Ref.
TEMPO	−0.24	HAT	[6]
Galactose Oxidase	-0.093	HAT	[7]
9,10-phenanthrenequinone (PQ)	-0.014	HAT	[8]
CuBr and tBuOOH	−0.31	HAT	[9]

Table S3. Literature reported for the Hydride transfer (HT) pathway using Hammett studies.

Catalyst	ρ value	Mechanism	Ref.
Au/Al_2O_3	-0.85	HT	[10]
Cytochrome P450	-0.6	HT	[11]
$Ru(OH)_x/Al_2O_3$	-0.46	HT	[12]
$[Cp^*IrCl_2]_2$	-0.92	HT	[13]

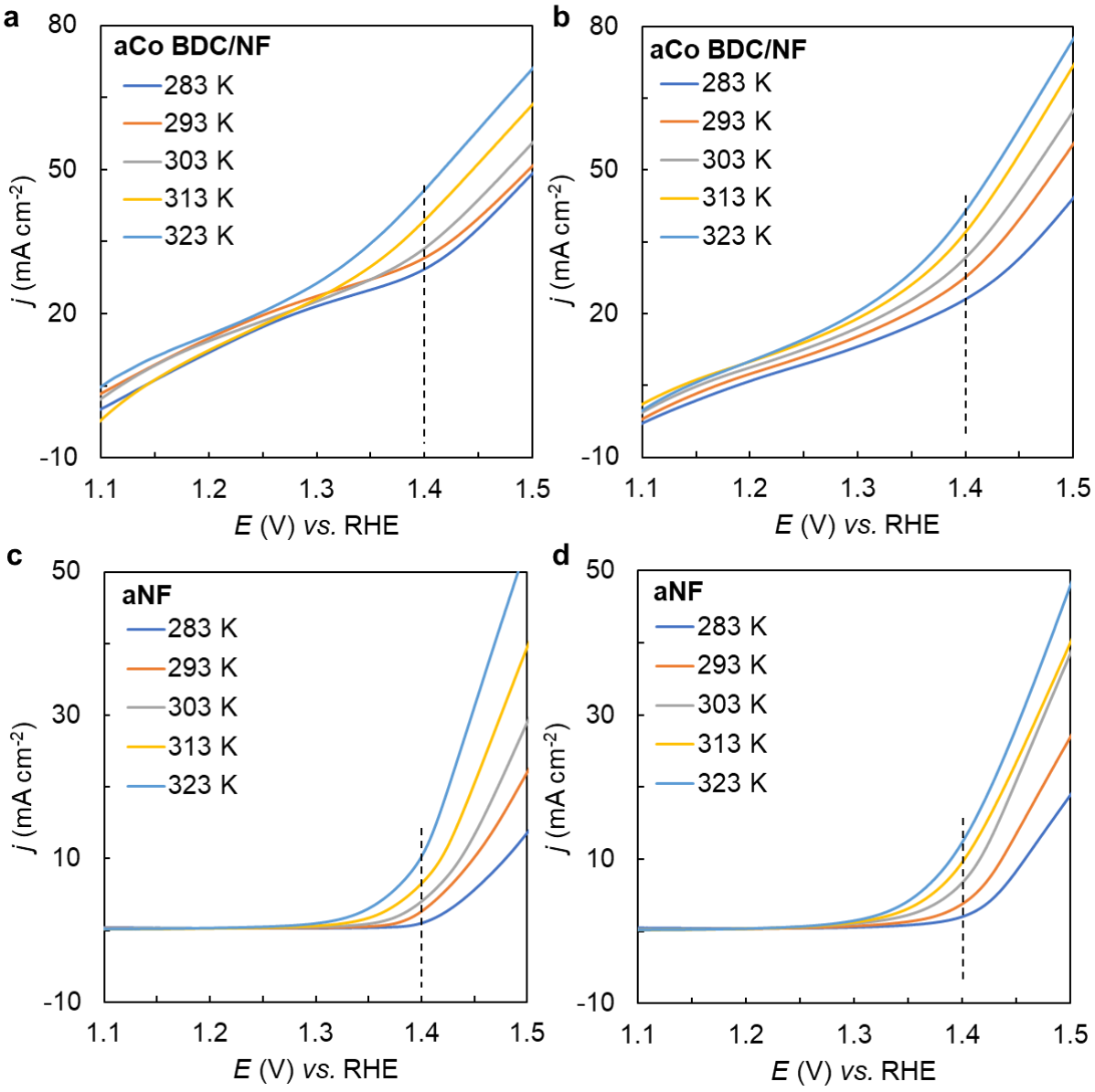

Figure S25. Eyring analysis of aCo BDC/NF and aNF for BAOR. LSVs of a) aCo BDC/NF; b) aCo BDC/NF; The observed negative current does not correspond to any reductive Faradaic reaction, but is instead attributed to double-layer relaxation and surface capacitive effects; c) aNF; d) aNF; for 100 mM BAOR; Variable temperature (T) = 283, 293, 303, 313, and 323 K; 0.5×0.5 cm^2 aCo BDC/NF or aNF as the working electrode, Pt as the counter electrode, and Ag/AgCl as the reference electrode in an undivided cell, at room temperature.

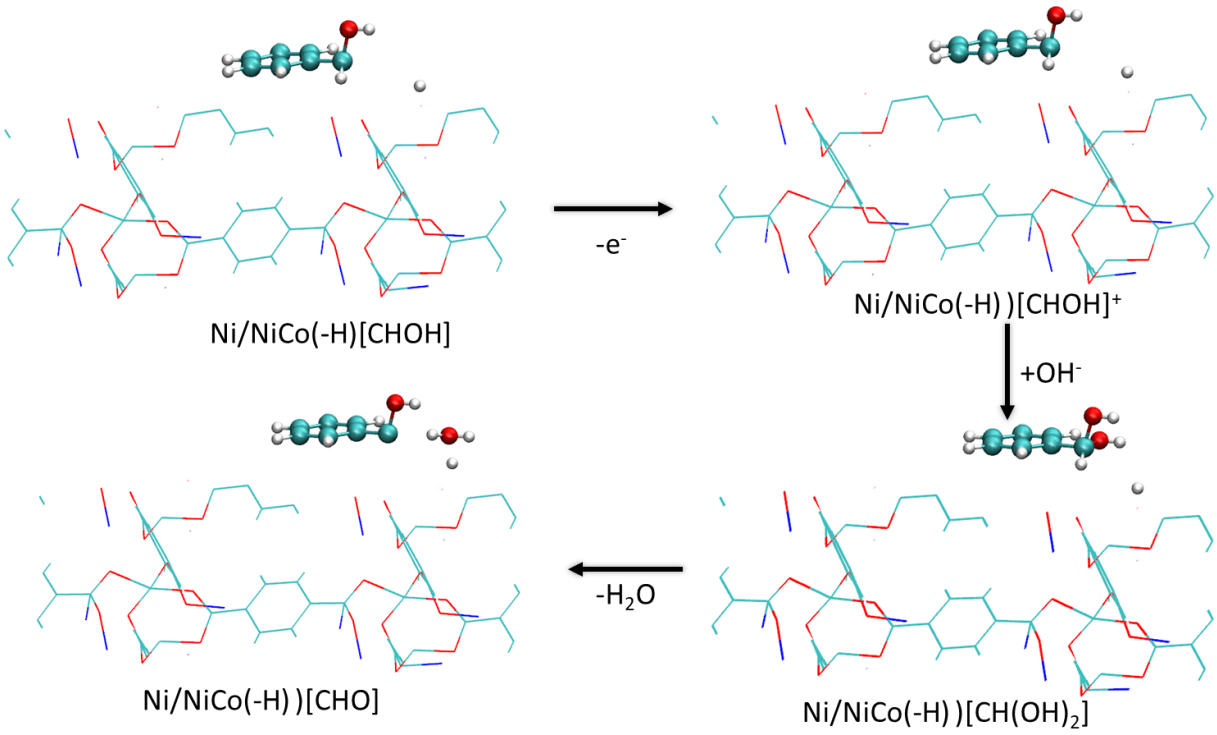

Figure S26. Reaction mechanism showing the stepwise transformation of benzyl alcohol into benzaldehyde. Benzyl alcohol oxidation pathways on (Co)Ni(O)OH.

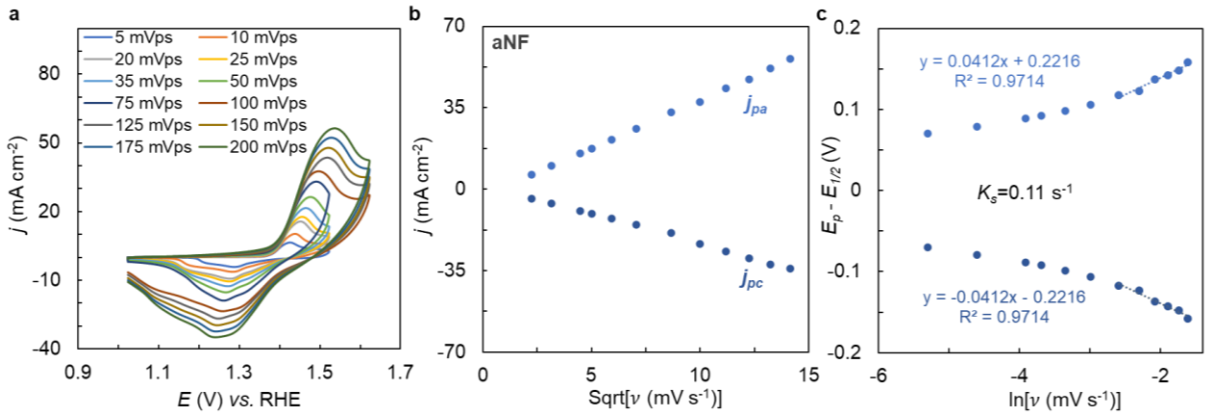

Figure S27. Analysis of Laviron equation for aNF. a) CV of aNF in 1M KOH; b) The plot of the oxidation and reduction peak current densities versus the square root of scan rates; c) k_s values of aNF; 0.5×0.5 cm^2 aNF as the working electrode, Pt as the counter electrode, and Ag/AgCl as the reference electrode in an undivided cell, at room temperature.

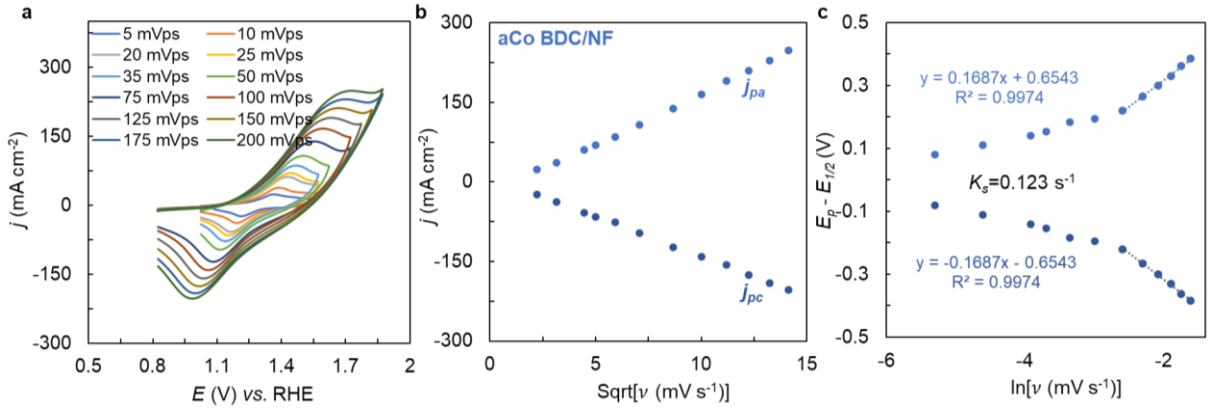

Figure S28. Analysis of Laviron equation for aCo BDC/NF. a) CV of aCo BDC/NF in 1M KOH; b) The plot of the oxidation and reduction peak current densities versus the square root of scan rates; c) k_s values of aCo BDC/NF; 0.5×0.5 cm^2 aCo BDC/NF as the working electrode, Pt as the counter electrode, and Ag/AgCl as the reference electrode in an undivided cell, at room temperature.

Table S4. Literature-reported redox rate constants (k_s).

Catalyst	k_s (s^{-1})	Condition	Ref.
PSCFM	0.17	1M KOH	[14]
PSCF	0.16	1M KOH	
Ce@$CoSe_2$/CC	0.271	1M KOH	[15]
$CoSe_2$/CC	0.266	1M KOH	
$Co(OH)_2$	0.2	1M KOH	[16]
Ag-$Co(OH)_2$	0.23	1M KOH	
Ni-OH/NF	0.252	1M KOH	[17]
NiCo-OH/NF	0.270	1M KOH	
NiFe-OH/NF	0.216	1M KOH	
NiCu-OH/NF	0.138	1M KOH	
Ov-LDH	0.108	1M KOH	[18]
S-Ov-LDH	0.125	1M KOH	
aCo BDC/NF	0.12	1M KOH	This Work
aNF	0.11	1M KOH	

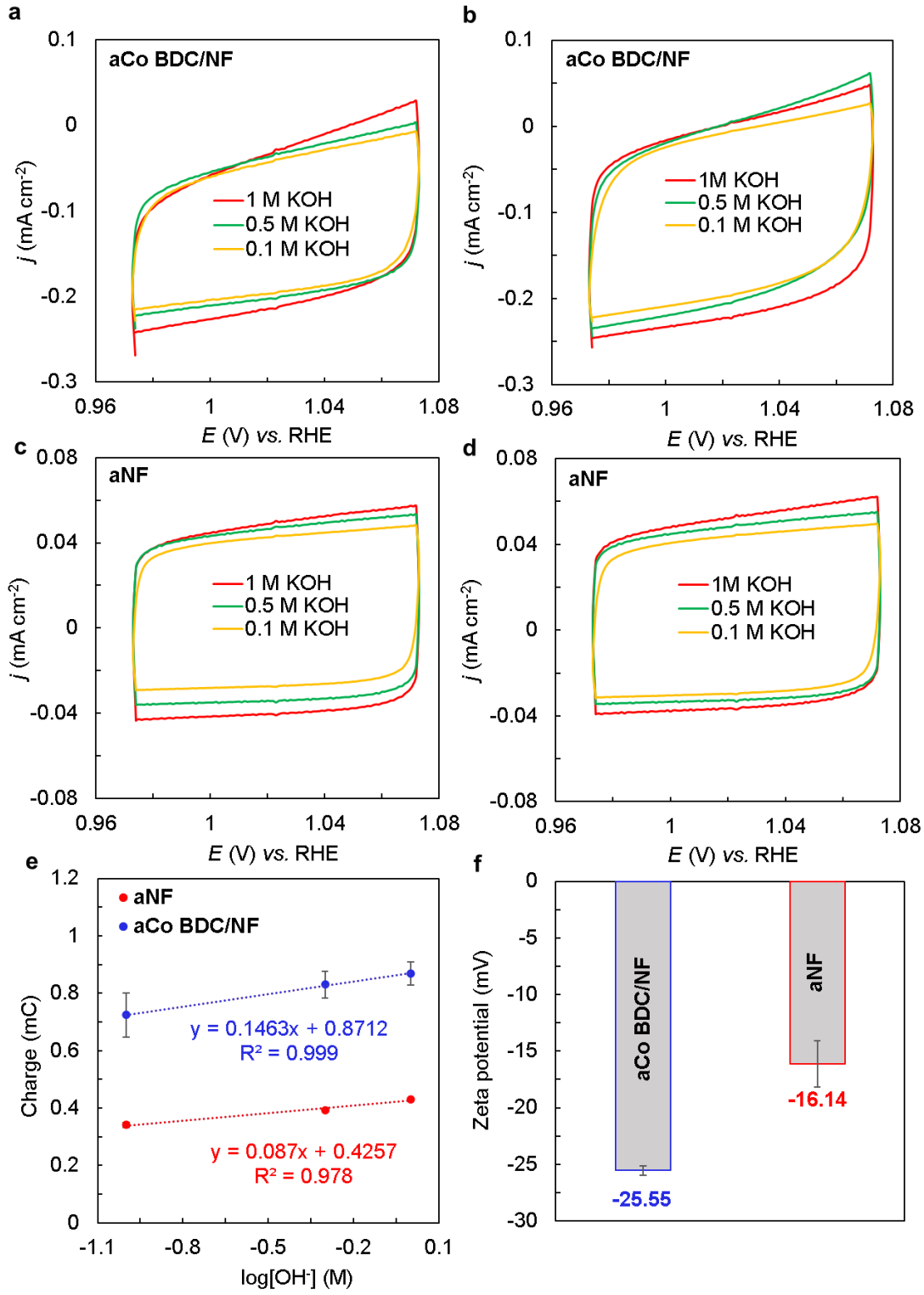

Figure 29. Electrochemical analysis related to OH^- adsorption capacity of aCo BDC/NF and aNF. CVs recorded at a scan rate of 20 mV s^{-1} in the non-Faradaic region in 1 M KOH for a, b) aCo BDC/NF and c, d) aNF; (e) CV charge as a function of log[OH^-]; (f) Zeta potential measurements of the catalysts.

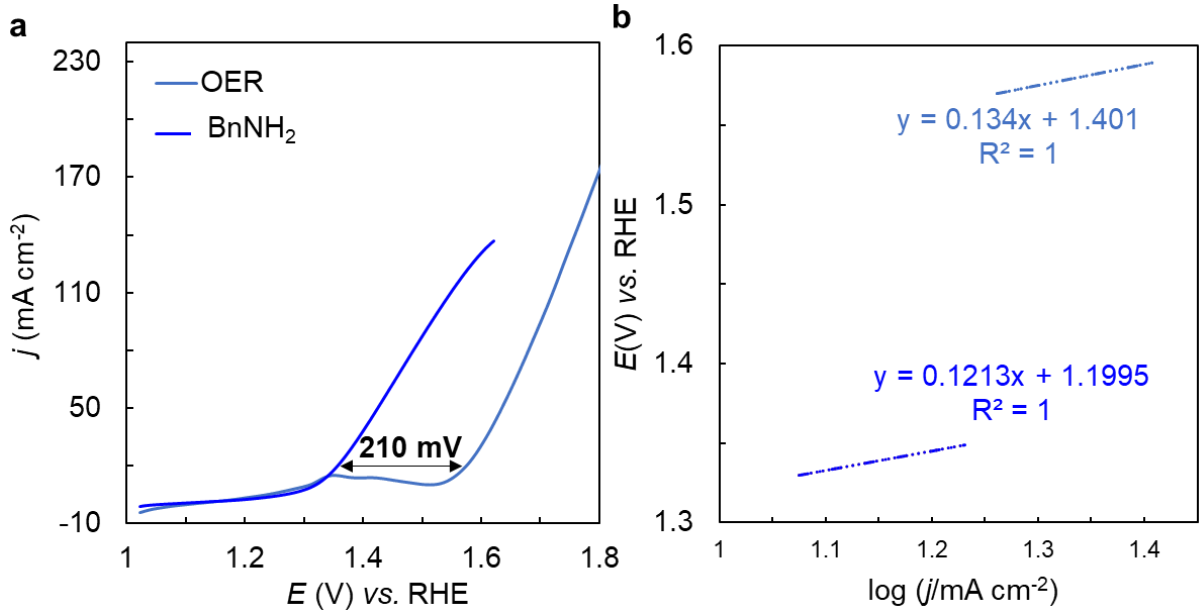

Figure S30. Catalyst comparison during Benzylamine ($BnNH_2$) oxidation and OER using aCo BDC/NF a) LSV; b) Tafel slope of OER and 100mM BAOR. No iR correction.

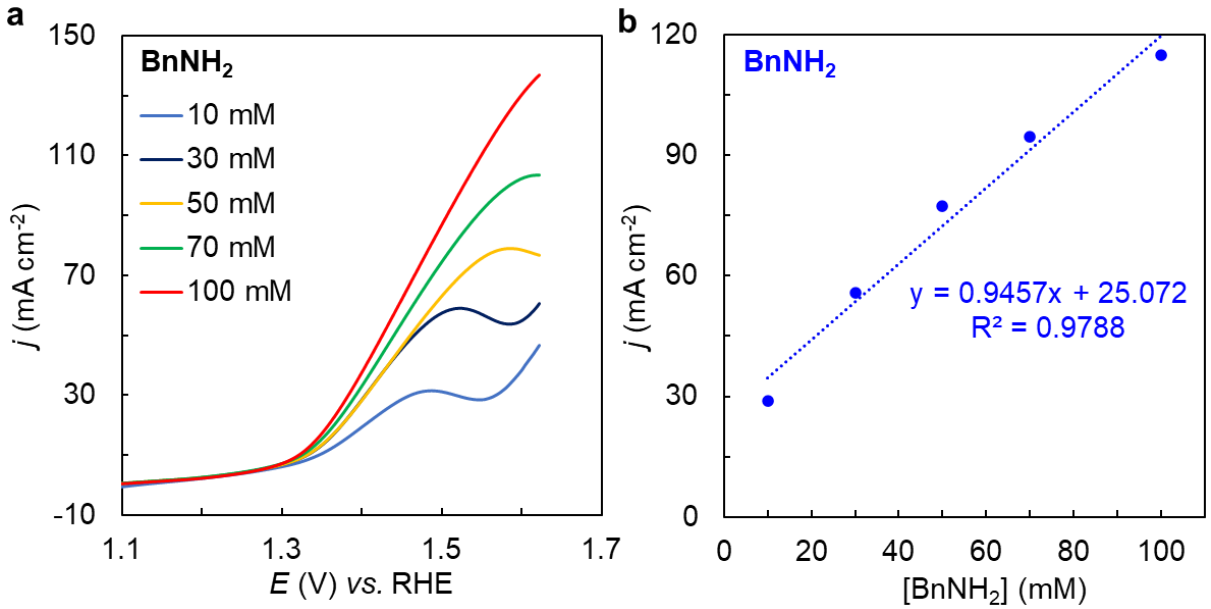

Figure S31. Electrochemical kinetic study of benzylamine oxidation by aCo BDC/NF. a) LSVs of varied benzylamine concentrations from 10 mM to 100 mM in 1 M KOH; b) Benzylamine concentration dependence comparison of aCo BDC/NF from 10 mM to 100 mM in 1 M KOH; 0.5×0.5 cm^2 activated Co BDC/NF as the working electrode, Pt as the counter electrode, and Ag/AgCl as the reference electrode in an undivided cell, at room temperature.

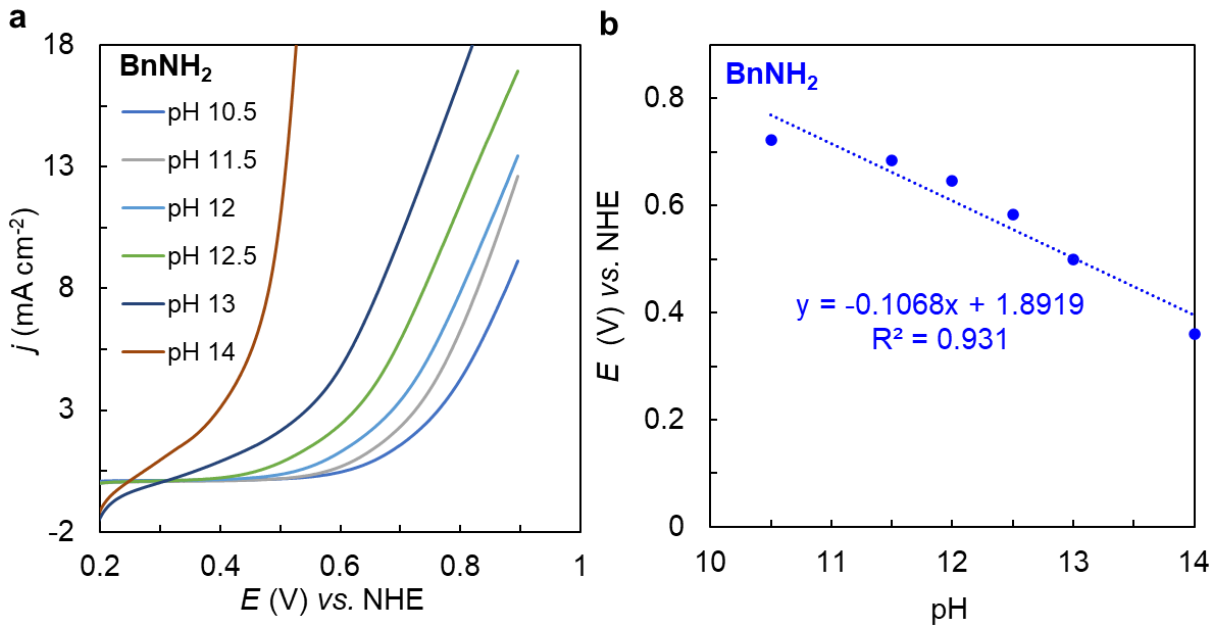

Figure S32. Electrochemical pH-dependence of benzylamine oxidation by aCo BDC/NF. a) LSVs of 100 mM benzylamine at different pH values; b) pH dependence comparison of aCo BDC/NF for 100 mM Benzylamine in 1 M KOH at different pH values (10.5, 11.5, 12, 12.5, 13 and 14); 0.5×0.5 cm^2 activated Co BDC/NF as the working electrode, Pt as the counter electrode, and Ag/AgCl as the reference electrode in an undivided cell, at room temperature.

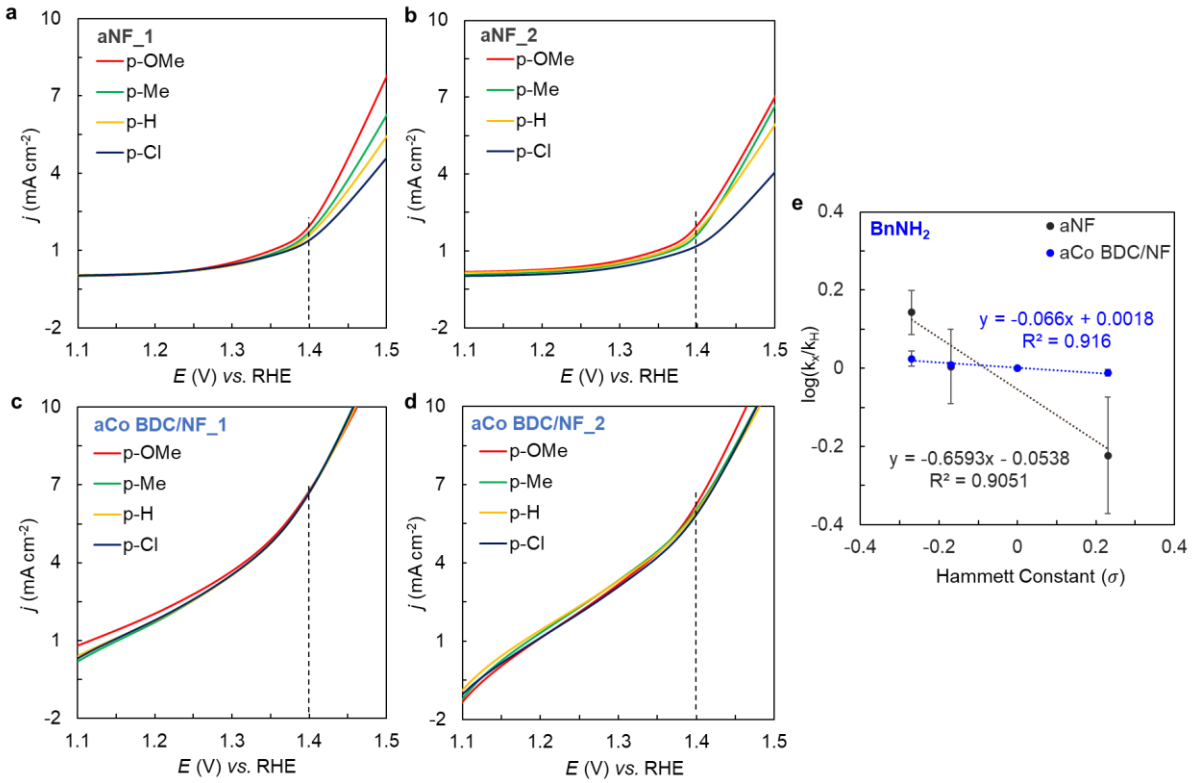

Figure S33. Hammett analysis of activated NF and aCo BDC/NF for benzylamine oxidation. LSVs of a) set-1of aNF; b) set-2 of aNF; c) set-1 of aCo BDC/NF; d) set-2 of aCo BDC/NF; for 100 mM BAOR with different *p*-substituents on BA in a mixed solvent (MeCN+H_2O+KOH) and Hammett analysis done at 1.4 V, 0.5×0.5 cm^2 aNF and aCo BDC/NF as the working electrode, Pt as the counter electrode, and Ag/AgCl as the reference electrode in an undivided cell, at room temperature. (σ Values of *p*-substituents -OMe, -Me, -H, and -Cl are -0.27, -0.17, 0, and 0.23, respectively) e) Hammett dependence comparison of aCo BDC/NF and aNF for 100 mM Benzylamine with different *p*-substituents (*p*-OMe, *p*-Me, *p*-H, and *p*-Cl) on $BnNH_2$ in a mixed solvent (MeCN+H_2O+KOH).

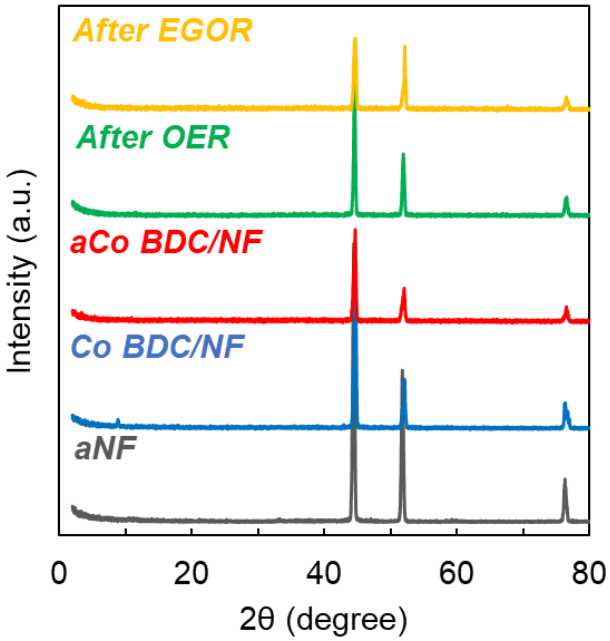

Figure S34. XRD pattern of the catalyst in different conditions. XRD pattern of aNF[4] (black), non-activated (blue), activated (red), after OER (green) and EGOR (yellow) of aCo BDC/ NF.

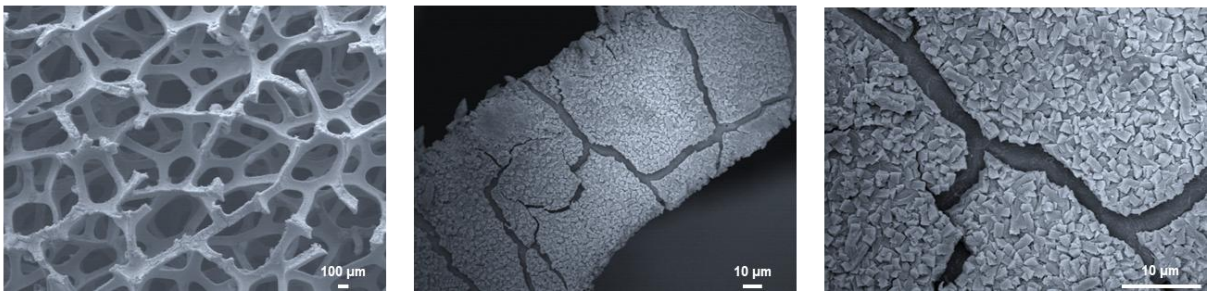

Figure S35. FE-SEM characterization of aCo BDC/NF after OER. FE-SEM images of aCo BDC/NF after OER at different magnifications.

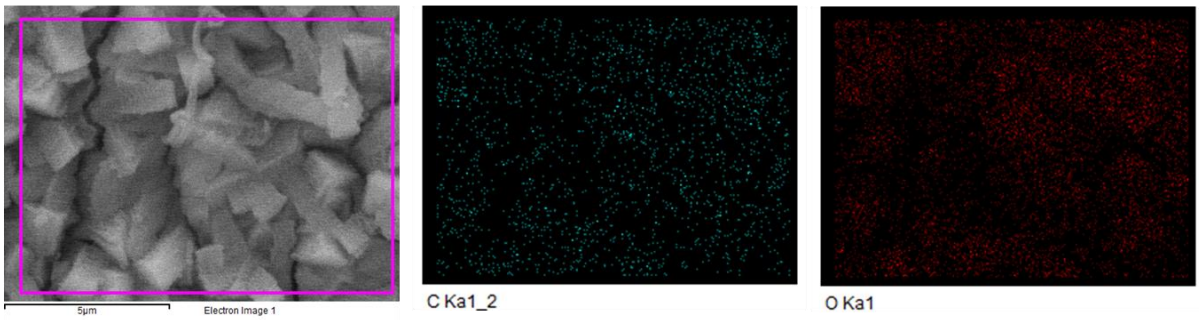

Element	Weight%	Atomic%
C K	9.17	23.66
O K	20.17	39.07
Co K	24.80	13.05
Ni K	45.87	24.22

Figure S36. Elemental mapping and EDS% composition (FE-SEM) characterization of aCo BDC/NF after OER. SEM data and corresponding element mapping: C: cyan, O: red, Co: magenta, Ni: green.

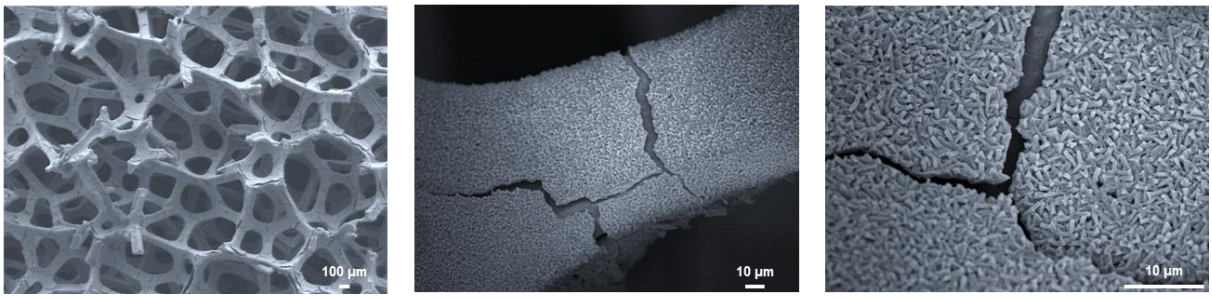

Figure S37. FE-SEM characterization of aCo BDC/NF after EGOR. FE-SEM images of aCo BDC/NF after EGOR at different magnifications.

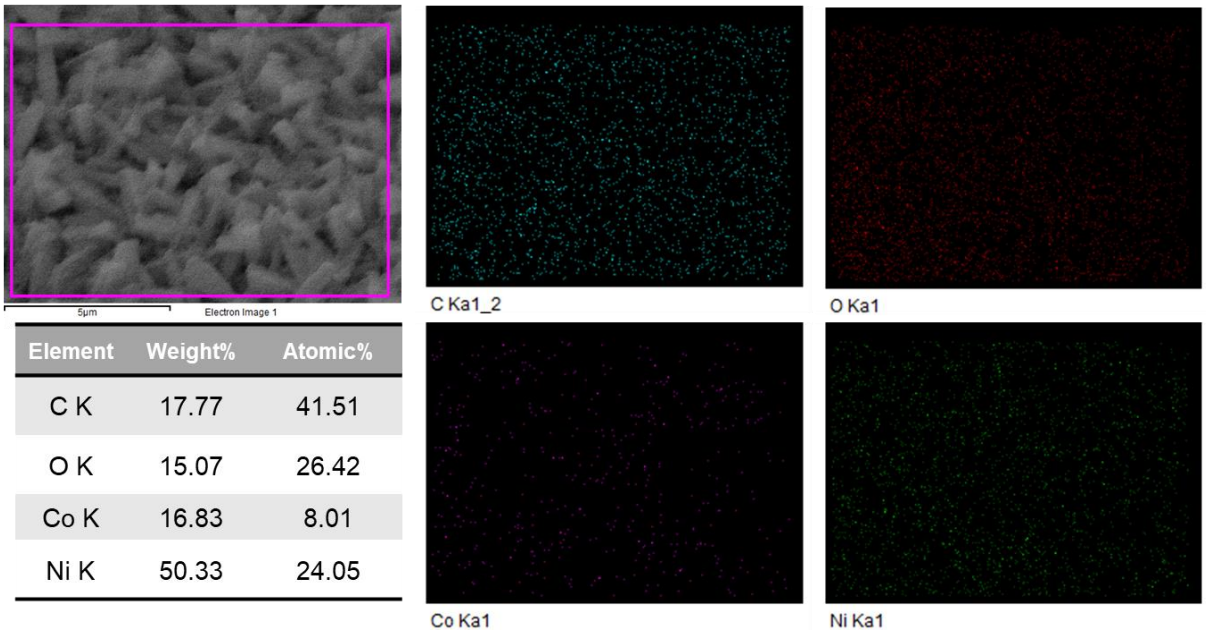

Element	Weight%	Atomic%
C K	17.77	41.51
O K	15.07	26.42
Co K	16.83	8.01
Ni K	50.33	24.05

Figure S38. Elemental mapping & EDS % composition (FE-SEM) characterization of aCo BDC/NF after EGOR. SEM data and corresponding element mapping: C: cyan, O: red, Co: magenta, Ni: green.

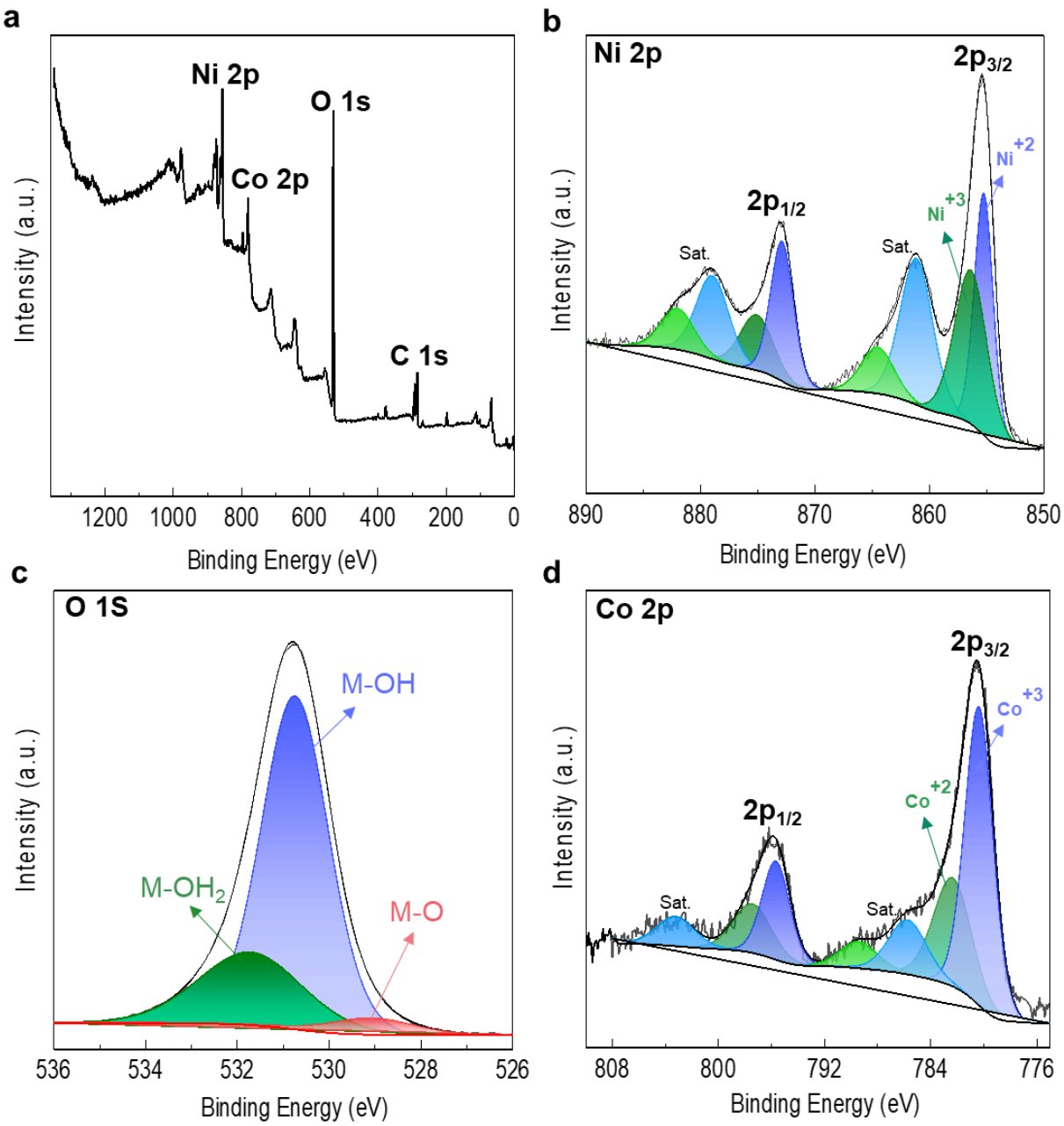

Figure S39. XPS spectra of aCo BDC/NF after EGOR. a) XPS survey spectra; b) XPS spectra of Ni 2p; c) XPS spectra of O 1s; d) XPS spectra of Co 2p; of aCo BDC/NF after EGOR.

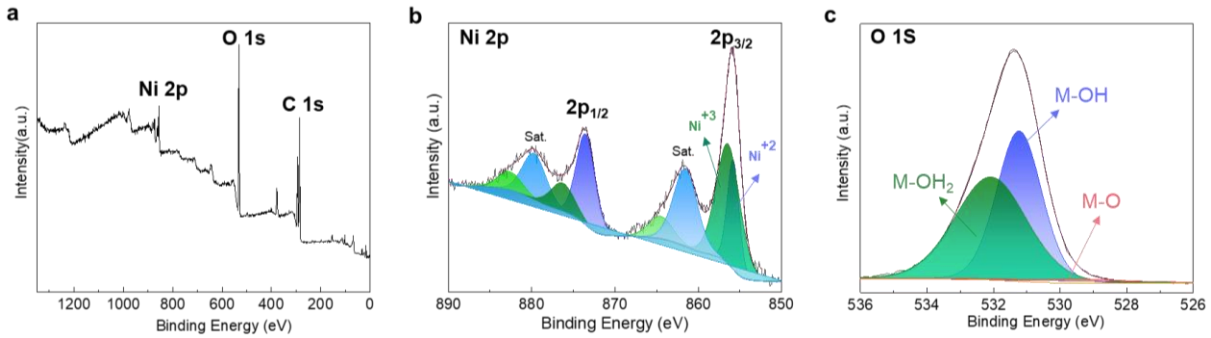

Figure S40. XPS spectra of aNF after EGOR. a) XPS survey spectra; b) XPS spectra of Ni 2p; c) XPS spectra of O 1s; of aNF after EGOR.

Supplementary note-6

Post-electrolysis characterization confirmed the elemental composition and oxidation states of the aNF catalyst after EGOR through XPS analysis **(Figures S37)**. The high-resolution XPS spectra show that for Ni 2p, peaks at 855.8 eV and 873.4 eV correspond to Ni^{2+}, while peaks at 856.4 eV and 876.2 eV indicate Ni^{3+}, confirming its presence **(Figure S37b)**. Additionally, broad satellite features are found between 861-865 eV and 878-882 eV, with a Ni^{3+}: Ni^{2+} area ratio of 2.2:1. The O 1s spectrum reveals peaks at 532.0 eV, 531.2 eV, and 529.5 eV, corresponding to M-OH_2, M-OH, and M-O species (M = Ni), with an area ratio of 1:0.9:0.04 **(Figure S37c)**.

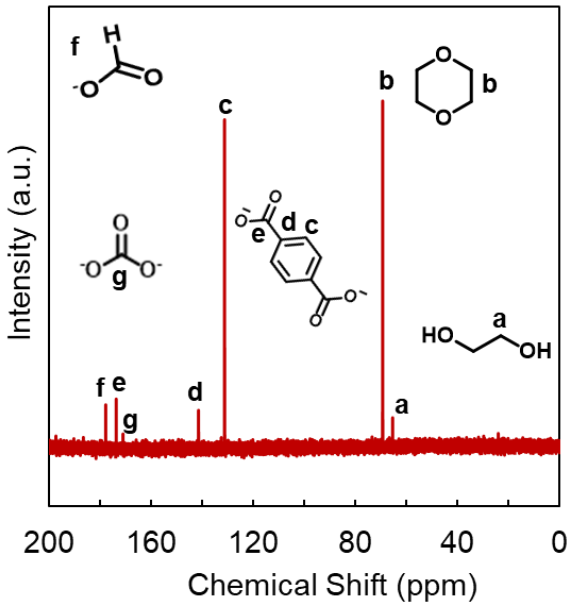

Figure S41. PET electrolysis product characterisation. a) ^{13}C-NMR spectrum of PET hydrolysate (0.4 mmol EG) oxidation after 3600 s.

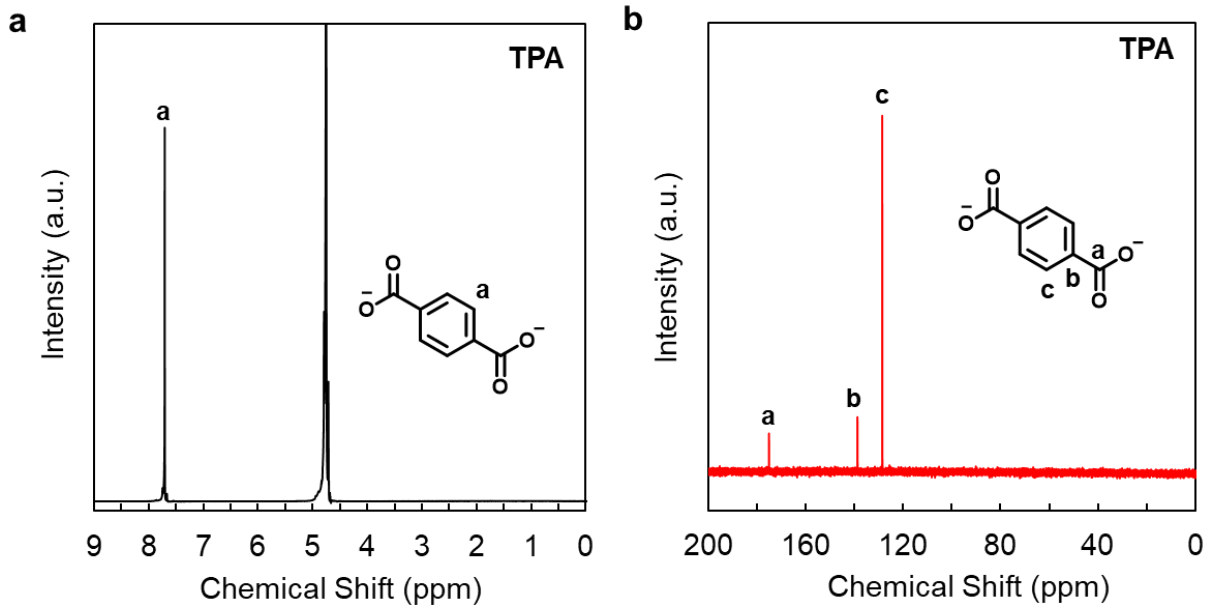

Figure S42. PET electrolysis product characterization. a) ^{1}H-NMR spectrum b) ^{13}C-NMR spectrum of the isolated terephthalic acid (TPA) after electrolysis. A 4 mL 1 M KOH aqueous solution was used as an electrolyte, and the electrolysis was performed at a constant current of 50 mA cm^{-2} in an undivided cell, at room temperature, and with constant stirring. NMR spectra are reported in D_2O solvent, and 1,4-dioxane (3.6 ppm) was used as the internal standard for the product quantification.

Table S5. Literature reports on electrochemical PET oxidation.

Plastic	Catalysis	Product	FE (%)	Ref.
PET hydrolysate	$CoNi_{0.25}$/NF	FA	95	[19]
PET hydrolysate	$CoNi_2P$	FA	85	[20]
PET hydrolysate	$NiCo_2O_4$/CFP	FA	90	[21]
PET hydrolysate	$CuCo_2O_4$/NF	FA	86	[22]
PET hydrolysate	NiCo-OH/NF	FA	92	[17]
PET hydrolysate	Ni-MOF@MnCo-OH	FA	90.7	[23]
PET hydrolysate	$Ni_{0.5}Ce_{0.5}Co_2O_4$	FA	95	[24]
PET hydrolysate	aCo BDC/NF	FA	81	This Work

Table S6. Summary of heterobimetallic Co-Ni catalysts on NF electrodes and key mechanistic insights from experimental studies.

Catalysis	Substrates	FE (%)	Mechanistic Insights from Experimental Studies	Ref.
BZ-NiCo(OH)x NiCO(OH)x	HMF	95.39	Active site Ni(O)OH: Identified using XPS, Raman. IHP: OCP drop experiment.	[25]
NiCo-S	HMF	96.4	DFT: Support the proposed reaction mechanism.	[26]
$Ni_{0.5}Ce_{0.5}Co_2O_{4-\delta}$	EG PET hydrolyzate	95	IHP: Laviron-derived k_s, OCP drop experiment, in-situ EIS. DFT: Support the proposed reaction mechanism.	[24]
NiCo-OH/NF	EG PET hydrolyzate	92	Active site Ni(O)OH: Identified using XPS, Raman. IHP: Laviron-derived k_s, OCP drop experiment, in-situ EIS. DFT: Support the proposed reaction mechanism.	[17]
Co-NiPxOy/NF	Methanol	90	Active site Ni(O)OH: Identified using XPS, Raman. IHP: OCP drop experiment, in-situ EIS. DFT: Support the proposed reaction mechanism.	[27]
Pd/NiCO-MOF/NF NiCo-MOF/NF	HMF	95	Active site Ni(O)OH: Identified using XPS, Raman, and OCP. IHP: OCP drop experiment, in-situ EIS. DFT: Support the proposed reaction mechanism.	[28]

aCo BDC/NF	Methanol EG BA HMF PET hydrolysate	84 99 91 85 92.6	**BDFE analysis:** Correlation between Ni^{3+}–O–H BDFE and alcohol BDFE (MeOH, EG, HMF, BA). **TON/TOF:** Calculated from Ni^{2+}/Ni^{3+} CV redox charge (surface-active sites). **Active site Ni(O)OH:** Identified using XPS, Raman, and OCP. **KIE & Tafel:** *C–H bond cleavage as RDS*; similar Tafel slopes indicate a common pathway. **Mechanism:** *Hammett analysis to distinguish HAT vs hydride transfer*. **Kinetics***: Eyring analysis* and Laviron (k_s) for IHP-related kinetics. **OH^- interaction:** Supported by redox charge, capacitance, zeta potential, and OCP for IHP **DFT calculations:** Support the proposed reaction mechanism **Application:** Demonstrated PET upcycling.	This Work

References

1 B. Zhu, B. Dong, F. Wang, Q. Yang, Y. He, C. Zhang, P. Jin and L. Feng, *Nat. Commun.*, DOI:10.1038/s41467-023-37441-9.

2 S. Behera, S. Dinda, R. Saha and B. Mondal, *ACS Catal.*, 2023, **13**, 469–474.

3 S. Behera, C. Chauhan and B. Mondal, *Small*, 2024, **20**, 1–7.

4 C. Chauhan, T. Gupta and B. Mondal, *Small*, 2025, **21**, 1–9.

5 T. Bligaard, J. K. Nørskov, S. Dahl, J. Matthiesen, C. H. Christensen and J. Sehested, 2004, **224**, 206–217.

6 A. Badalyan and S. S. Stahl, *Nature*, 2016, **535**, 406–410.

7 M. M. Whittaker and J. W. Whittaker, *Biochemistry*, 2001, **40**, 7140–7148.

8 J. Talvitie, I. Alanko, A. Lenarda, N. Durandin, N. Tkachenko, M. Nieger and J. Helaja, *ChemPhotoChem*, 2023, **7**, 1–9.

9 E. Boess, L. M. Wolf, S. Malakar, M. Salamone, M. Bietti, W. Thiel and M. Klussmann, *ACS Catal.*, 2016, **6**, 3253–3261.

10 G. Kumar, L. Tibbitts, J. Newell, B. Panthi, A. Mukhopadhyay, R. M. Rioux, C. J. Pursell, M. Janik and B. D. Chandler, *Nat. Chem.*, 2018, **10**, 268–274.

11 M. A. Cerny and R. P. Hanzlik, *J. Am. Chem. Soc.*, 2006, **128**, 3346–3354.

12 T. Oishi, K. Yamaguchi and N. Mizuno, *Top. Catal.*, 2010, **53**, 479–486.

13 P. Fristrup, M. Tursky and R. Madsen, *Org. Biomol. Chem.*, 2012, **10**, 2569–2577.

14 C. Jiang, H. He, H. Guo, X. Zhang, Q. Han, Y. Weng, X. Fu, Y. Zhu, N. Yan, X. Tu and Y. Sun, *Nat. Commun.*, DOI:10.1038/s41467-024-50605-5.

15 Q. Guo, Y. Li, Z. Xu and R. Liu, *Adv. Energy Mater.*, 2025, **15**, 1–11.

16 P. Zhou, X. Lv, H. Huang, B. Cheng, H. Zhan, Y. Lu, T. Frauenheim, S. Wang and Y. Zou, *Adv. Mater.*, 2024, **36**, 1–11.

17 X. Zhao, C. Kuang, C. An and M. Wang, *Chem. Eng. J.*, 2024, **500**, 157275.

18 B. Cheng, H. Zhan, Y. Lu, D. Xing, X. Lv, T. Frauenheim, P. Zhou, S. Wang and Y. Zou, *Adv. Sci.*, 2024, **11**, 1–10.

19 Y. Li, L. Q. Lee, Z. G. Yu, H. Zhao, Y. W. Zhang, P. Gao and H. Li, *Sustain. Energy Fuels*, 2022, **6**, 4916–4924.

20 X. H. Wang, Z. N. Zhang, Z. Wang, Y. Ding, Q. G. Zhai, Y. C. Jiang, S. N. Li and Y. Chen, *Chem. Eng. J.*, 2023, **465**, 142938.

21 J. Wang, X. Li, M. Wang, T. Zhang, X. Chai, J. Lu, T. Wang, Y. Zhao and D. Ma, *ACS Catal.*, 2022, **12**, 6722–6728.

22 F. Liu, X. Gao, R. Shi, E. C. M. Tse and Y. Chen, *Green Chem.*, 2022, **24**, 6571–6577.

23 W. Li, D. Xiao, X. Gong, X. Xu, F. Ma, Z. Wang, P. Wang, Y. Liu, Y. Dai, Z. Zheng, Y. Fan and B. Huang, *Chem. Eng. J.*, DOI:10.1016/j.cej.2023.148087.

24 Z. Li, Z. Yang, S. Wang, H. Luo, Z. Xue, Z. Liu and T. Mu, *Chem. Eng. J.*, 2024, **479**, 147611.

25 X. Liu, X. Wang, C. Mao, J. Qiu, R. Wang, Y. Liu, Y. Chen and D. Wang, .

26 Z. Zhao, T. Guo, X. Luo, X. Qin, L. Zheng, L. Yu, Z. Lv and H. Zheng, 2022, 3817–3825.

27 J. Shen, C. Hong, Y. Qi, Y. Zhu, H. Jiang and C. Li, 2025, **2503950**, 1–13.

28 Z. Liu, C. Xie, Y. Zhong and L. Yu, 2026, 11443–11455.